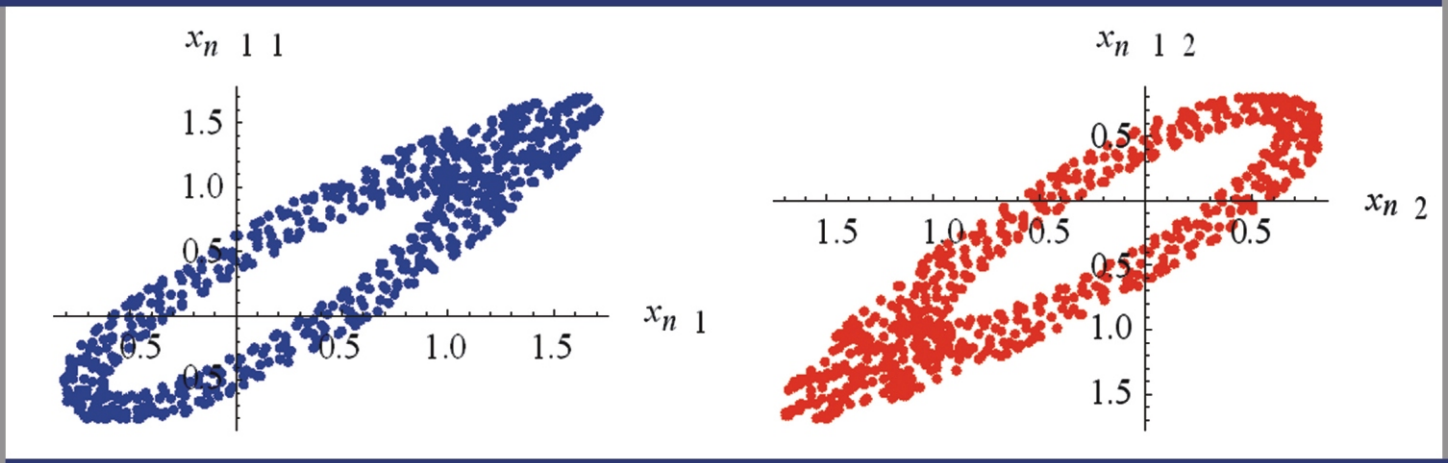

Journal of Electromagnetic Analysis and Applications

ISSN: 1942-0730

Volume 2, Number 10, October 2010

www.scirp.org/journal/jemaa

Scientific Research

ISSN: 1942-0730

9 771942 073001 10

JOURNAL EDITORIAL BOARD

ISSN: 1942-0730 (Print) 1942-0749 (Online)

http://www.scirp.org/journal/jemaa

J. Electromagnetic Analysis & Applications, 2010, 2, 581-606
Published Online October 2010 in SciRes (http://www.SciRP.org/journal/jemaa/)

TABLE OF CONTENTS

Volume 2 Number 10 October 2010

Journal of Electromagnetic Analysis and Applications (JEMAA)

Journal Information

SUBSCRIPTIONS

The *Journal of Electromagnetic Analysis and Applications* (Online at Scientific Research Publishing, www.SciRP.org) is published monthly by Scientific Research Publishing, Inc., USA.

Subscription rates:

Print: $50 per issue.
To subscribe, please contact Journals Subscriptions Department, E-mail: sub@scirp.org

SERVICES

Advertisements
Advertisement Sales Department, E-mail: service@scirp.org

Reprints (minimum quantity 100 copies)
Reprints Co-ordinator, Scientific Research Publishing, Inc., USA.
E-mail: sub@scirp.org

COPYRIGHT

PRODUCTION INFORMATION

For manuscripts that have been accepted for publication, please contact:
E-mail: jemaa@scirp.org

J. Electromagnetic Analysis & Applications, 2010, 2, 581-587
doi:10.4236/jemaa.2010.210075 Published Online October 2010 (http://www.SciRP.org/journal/jemaa)

Effects of Thermal Diffusion and Chemical Reaction on MHD Flow of Dusty Visco-Elastic (Walter's Liquid Model-B) Fluid

Om Prakash[1], Devendra Kumar[1], Y. K. Dwivedi[2]

[1]Department of Mathematics, Hindustan College of Science and technology, Farah Mathura (U.P.)-India; [2]Department of Mathematics, Ganjdundwara P.G. College Ganjdundwara, Kashiram Nagar (U.P.)-India.
Email: op_ibs@rediffmail.com

Received May 20th, 2010; revised July 26th, 2010; accepted September 19th, 2010.

ABSTRACT

The present note consists, the effects of thermal diffusion and chemical reaction on MHD flow of dusty viscous incompressible, electrically conducting fluid between two vertical heated, porous, parallel plates with heat source/sink. The plate temperature is raised linearly with time and concentration level near the plate to C_w. The variable temperature and uniform mass diffusion taking into account the chemical reaction of first order. The series solution method is used to solve the mathematical equations. Effects of various parameters like chemical reaction (K), thermal diffusion (S_T) and magnetic field (M) etc. on velocity profile, skin friction, concentration profile and temperature field are displayed graphically and discussed numerically for different physical parameters. The analysis developed here for thermal diffusion, bears good agreement with real life problems.

Keywords: *MHD Flow, Thermal Diffusion* (*Soret Effect*), *Heat Source/Sink, Skin Friction*

1. Introduction

Many transport processes exist in nature and industrial application in which the transfer of heat and mass occurs simultaneously as a result of combined buoyancy effects of thermal diffusion and diffusion of chemical species. In the last few decades several efforts have been made to solve the problems on heat and mass transfer in view of their application to astrophysics, geophysics and engineering.

Chemical reaction can be codified either heterogeneous or homogeneous processes. Its effect depends on the nature of the reaction whether the reaction is heterogeneous or homogeneous. A reaction is of order n, if the reaction rate is proportional to the n^{th} power of concentration. In particular, a reaction is of first order, if the rate of reaction is directly proportional to concentration itself. Experimental and theoretical works on MHD flow with thermal diffusion and chemical reaction have been done extensively in various areas *i.e.* sustain plasma confinement for controlled thermo nuclear fusion, liquid metal cooling of nuclear reactions and electromagnetic casting of metals. Chambre and Yang [1] have worked on thermal diffusion of a chemically reactive species in a laminar boundary layer flow. Dusty viscous and visco-elastic fluids have been discussed by Saffman [2], Micheal and Norey [3], Raptis and Perdikis [4]. Singh [5] proposed the study of free convection and mass diffusion of a dusty visco-elastic (Walter's Liquid Model-B) fluid flowing between two heated porous plates in porous media in presence of magnetic field. References [6,7] focused on the study of convective heat and mass transfer incompressible, viscous Boussinesq fluid in presence of chemical reaction of first order. References [8-10] discussed the effects of thermo diffusion (Soret effects) and diffusion-thermo (Dufour effects) on MHD mixed convection heat and mass transfer of an electrically conducting fluid. Mahantesh *et al.* [11] studied the boundary layer flow behavior and heat transfer characteristic in Walter's liquid model-B fluid flow. Sharma *et al*. [12] discussed the unsteady MHD free convection heat and mass transfer of viscous fluid flowing through a Darcian porous regime adjacent to a moving vertical semi-infinite plate under Soret and Dufour effect.

Recently Kumar and Srivastava [13] examined the effects of chemical reaction on MHD flow of dusty visco-elastic (Walters's liquid model-B) liquid with heat source/

sink. The interest of present investigation is to obtain analytical expressions for various profiles like velocity, skin friction for dusty fluid as well as dust particles and also temperature, concentration for dusty fluid. The effects of thermal diffusion parameter (Soret number), chemical reaction parameter etc. are discussed for different profiles.

2. Nomenclature

$B_{0:}$ Magnetic field
m: Magnetic field Parameter
C : Species concentration in the field
P_r : Prandtl Number
C_w: Concentration of the plate
S_c : Schmidt Number
C_0: Initial uniform concentration at T_0
T_w: Plate temperature
C_p: Specific heat at constant pressure
T_0: Initial temperature
G : Acceleration due to gravity
t : Time
G_r: Thermal Grashof number
u, v: Velocities of dusty fluid and dust particle respectively
S : Source/sink parameter respectively in the x-direction
G_m: modified Grashof number
y : Co-ordinate axes as in normal to the plate
K : dimensionless chemical reaction parameter
A : Decay factor
K_1: Chemical reaction parameter
D_T: Thermal diffusion coefficient

3. Mathematical Formulation

We consider the effects of thermal diffusion and chemical reaction on the unsteady dusty flow of an incompressible, slightly conducting, visco-elastic fluid between two heated porous infinite parallel plates (distance 2 h apart) under the influence of uniform magnetic field normal to the flow field in presence of heat source/sink. We assume x-axis along the flow in the mid-way of the plates and y-axis perpendicular to it. Let u, v be the velocities of dusty fluid and dust particles respectively in the direction of x-axis. The present analysis is based on the following assumptions:

1) The flow is in the direction of x-axis and is driven by a constant pressure $\partial p/\partial x$ with negligible body forces.

2) The dust particles are non-conducting, solid, spherical, and equal in size, uniformly and symmetrically distributed in the flow field and their number density N_0 is constant throughout the motion.

3) There is no externally applied electric field and the induced magnetic field is negligible.

4) Initially, when $t \le 0$, the channel, walls as well as dusty fluid are assumed to be at the same temperature T_0. The foreign mass is assumed to be present at low level and it is uniformly distributed such that it is everywhere C_0.

5) When t > 0, the temperature of the walls is instantaneously raised to T_W and the species concentration is raised to C_W.

6) There exists a chemical reaction in the mixture.

Under these assumptions and Boussinesq's approximation with concentration, the equations governing the flow are:

$$\frac{\partial u}{\partial t} = g\beta(T-T_0) + g\beta'(C-C_0) + \nu(1-K_0\frac{\partial}{\partial t})\frac{\partial^2 u}{\partial y^2} + \frac{KN_0}{\rho}(v-u) - \frac{\sigma}{\rho}B_0^2 u - \frac{\nu}{K}u \quad \ldots.(1)$$

$$m\frac{\partial v}{\partial t} = K'(u-v) \quad (2)$$

$$\frac{\partial T}{\partial t} = \frac{K_T}{\rho C_p}\frac{\partial^2 T}{\partial^2 y} - \frac{Q}{\rho C_p}(T-T_0) \quad (3)$$

$$\frac{\partial C}{\partial t} = D\frac{\partial^2 C}{\partial^2 y} - K_1(C-C_0) + D_T\frac{\partial^2 T}{\partial^2 y} \quad (4)$$

(where the symbols have their usual meaning), at t = 0, the temperature and concentration level changes according to the following laws:

$$T = T_0 + (T_w - T_0)(1-e^{-at})$$

$$C = C_0 + (C_w - C_0)(1-e^{-at})$$

The initial and boundary conditions relevant to the problem are:

$$\text{t} = 0\text{: u} = 0 = \text{v, T} = \text{T}_0 \quad y \in (-d, d)$$

$$\text{t} > 0\text{: u} = 0 = \text{v}, \quad T = T_0 + (T_w - T_0)(1-e^{-at}),$$

$$C = C_0 + (C_w - C_0)(1-e^{-at}) \quad \text{for y} = -\text{d}$$

$$\text{u} = 0 = \text{v}, \quad T = T_0 + (T_w - T_0)(1-e^{-at}),$$

$$C = C_0 + (C_w - C_0)(1-e^{-at}) \quad \text{for y = d} \quad (5)$$

We introduce the following non-dimensional quantities,

$$y^* = \frac{y}{d}, u^* = \frac{u}{d}, v^* = \frac{v}{d}, T = \frac{T-T_0}{T_w - T_0},$$

$$C^* = \frac{C-C_0}{C_w - C_0}, t^* = \frac{vt}{d^2}, a^* = \frac{d^2 a}{\nu}$$

Introducing these non-dimensional quantities, Equations (1), (2), (3) & (4) reduce to

$$\frac{\partial u}{\partial t} = G_r T + G_m C + (1 - E\frac{\partial}{\partial t})\frac{\partial^2 u}{\partial y^2} + \frac{\lambda}{w}(v-u) - \frac{u}{K_1} - M^2 u \quad (6)$$

$$W\frac{\partial v}{\partial t} = (u - v) \quad (7)$$

$$\frac{\partial^2 T}{\partial^2 y} - P_r\frac{\partial T}{\partial t} - ST = 0 \quad (8)$$

$$\frac{\partial^2 C}{\partial^2 y} - S_c\frac{\partial C}{\partial t} - KS_c C + S_T\frac{\partial^2 T}{\partial^2 y} = 0 \quad (9)$$

Now initial and boundary condition (5) according to new system become,

T = 0: u = 0 = v, T = 0 $y \in (-1,1)$

t > 0: u = 0 = v, T = 1 – e^{-at}, C = 1 – e^{-at}, for y = –1

u = 0 = v, T = 1 – e^{-at}, C = 1 – e^{-at}, for y = 1 (10)

where, $\lambda = \frac{mN_0}{\rho}$ (mass concentration of dust particle)

M (Hartmann number) $= B_0 d\sqrt{\frac{\sigma}{\mu}}$

W (relaxation time parameter for particles) $= \frac{m\nu}{K' d^2}$

G_r (grashof number) $= \frac{g\beta d(T_w - T_0)}{\nu}$

G_m (Modified grashof number) $= \frac{g\beta' d(C_w - C_0)}{\nu}$

S_c (Schmidt number) $= \frac{\nu}{D}$

S (heat source/sink parameter) $= Q\frac{d^2}{K_T}$

K (Chemical reaction parameter) $= \frac{K_1 d^2}{\nu}$

$E = \frac{K_0\nu}{d^2}$ (Visco-elastic parameter), $K_1 = \frac{k}{d^2}$, P_r (Prandtl number) $= \frac{\mu C_p}{K_T}$

$S_T = \frac{D_T}{D}\frac{(T_w - T_0)}{(C_w - C_0)}$ (Thermal diffusion parameter)

4. Method of Solution

To solve the Equations (6) to (9) subject to the boundary conditions (10), according to I. Pop [14], we assume

$$u(y,t) = u_0(y) + \varepsilon u_1(y,t)e^{-at} + \ldots\ldots\ldots\ldots$$

$$v(y,t) = v_0(y) + \varepsilon v_1(y,t)e^{-at} + \ldots\ldots\ldots\ldots$$

$$T(y,t) = T_0(y) + \varepsilon T_1(y,t)e^{-at} + \ldots\ldots\ldots\ldots$$

$$C(y,t) = C_0(y) + \varepsilon C_1(y,t)e^{-at} + \ldots\ldots\ldots\ldots \quad (11)$$

Substituting the equations like (11) into the Equations (6) to (9) and equating harmonic and non-harmonic terms, we get the following set of equations.

$$u_0'' - (\frac{1}{K_1} + M_1^2)u_0 = -G_r T_0 - G_m C_0 \quad (12)$$

$$(1+aE)u_1'' + \frac{\lambda}{w}u_1 - (\frac{1}{K_1} + M_1^2 - a)u_1 - \frac{\lambda}{w}v_1 = -G_r T_1 - G_m C_1 \quad (13)$$

$u_0 = v_0$ & $u_1 = v_1$ (1-aw) (14)

$T_0'' - ST_0 = 0$ (15)

$T_1'' -$ (S-aPr) $T_1 = 0$ (16)

$$C_0'' - KS_c C_0 + S_T T_0'' = 0 \quad (17)$$

$$C_1'' - (K-a)S_c C_1 + S_T T_1'' = 0 \quad (18)$$

Where dashes represents differentiation w. r. to y.

Boundary conditions are reduced to:

$$u_0 = v_0 = u_1 = v_1,\ T_0 = C_0 = 1,\quad T_1 = C_1 = -\frac{1}{\varepsilon},\ at\ y = -1$$
$$u_0 = v_0 = u_1 = v_1,\ T_0 = C_0 = 1,\quad T_1 = C_1 = -\frac{1}{\varepsilon},\ at\ y = 1 \quad (19)$$

Solutions of the Equations (12) to (18) under the boundary conditions (19) after substituting in (11), we have:

$$u(y,t) = (A_{11}+A_{12})\frac{CoshM_1 y}{CoshM_1} - A_{11}\frac{CoshAy}{CoshA} - A_{12}\frac{CoshA_0 y}{CoshA_0} + \left\{-(A_{13}+A_{14})\frac{CoshM_2 y}{CoshM_2} + A_{13}\frac{CoshA_1 y}{CoshA_1} + A_{14}\frac{CoshA_2 y}{CoshA_2}\right\}e^{-at}$$

$$V(y,t) = (A_{11}+A_{12})\frac{CoshM_1 y}{CoshM_1} - A_{11}\frac{CoshAy}{CoshA} - A_{12}\frac{CoshA_0 y}{CoshA_0} + \left(\frac{1}{1-aw}\right)\left\{-(A_{13}+A_{14})\frac{CoshM_2 y}{CoshM_2} + A_{13}\frac{CoshA_1 y}{CoshA_1} + A_{14}\frac{CoshA_2 y}{CoshA_2}\right\}e^{-at}$$

$$C(y,t) = (1-A_m)\frac{CoshA_0 y}{CoshA_0} + A_m\frac{CoshAy}{CoshA} + \left\{(A_n - 1)\frac{CoshA_2 y}{CoshA_2} - A_n\frac{CoshA_1 y}{CoshA_1}\right\}e^{-at}$$

$$T(y,t) = \frac{CoshAy}{CoshA} - \frac{CoshA_1 y}{CoshA_1} e^{-at}$$

4.1. Skin Friction

Let τ_f and τ_p be the skin friction for dusty fluid and dust particles respectively then we have:

$$\tau_f = \left|\frac{\partial u}{\partial y}\right|_{y=1} = (A_{11} + A_{12}).M_1 \tanh M_1 - A_{11} A \tanh A -$$
$$A_{12} A_0 \tanh A_0 + [-(A_{13} + A_{14})M_2 \tanh M_2 +$$
$$A_{13} A_1 tanh A_1 + A_{14} A_2 \tanh A_2]e^{-at}$$

$$\tau_p = \left|\frac{\partial v}{\partial y}\right|_{y=1} = (A_{11} + A_{12})M_1 \tanh M_1 - A_{11} A \tanh A -$$
$$A_{12} A_0 \tanh A_0 + \left(\frac{1}{1-aw}\right)[-(A_{13} + A_{14})M_2 \tanh M_2 +$$
$$A_{13} A_1 tanh A_1 + A_{14} A_2 \tanh A_2]e^{-at}$$

4.2. Appendix

$$A = \sqrt{S}\ ,\ A_0 = \sqrt{KS_c}\ ,\ A_1 = \sqrt{S - aP_r}\ ,\ A_2 = \sqrt{(K-a)S_c}\ ,$$
$$S_T = \frac{D_T(T_W - T_0)}{D(C_W - C_0)}\ ,\ M_1^2 = \left[M^2 + \frac{1}{K_1}\right],$$
$$M_2^2 = \frac{1}{1+aE}\left[M^2 + \frac{1}{K^2_1} - a - \frac{al}{1-aw}\right],$$
$$A_m = \frac{S_T.A^2}{A_1^2 - A_2^2}\ ,\ A_n = \frac{S_T.A^2}{A^2 - A_0^2}\ ,\ A_{11} = \frac{G_r + G_m.A_m}{A^2 - M_1^2}\ ,$$
$$A_{12} = \frac{G_m(1-A_m)}{A_0^2 - M_1^2}\ ,\ A_{13} = \frac{G_r + G_m.A_n}{A_1^2 - M_1^2}\ ,\ A_{14} = \frac{G_m(1-A_n)}{A_2^2 - M_2^2}$$

5. Results & Discussion

Numerical solutions for velocity profile, skin friction for dusty fluid as well as dust particles and also temperature field, concentration profile for dusty fluid have been calculated. The values of different parameters and their effects on velocity, Temperature, concentration and skin friction have been displayed through graphs.

A temperature field has been represented in **Figure 1**, which indicates the effects of heat source/sink parameter and Prandtl number.

5.1. Temperature Field for Different Values of S and P_r (t = 1, a = 0.2)

It is observed that increasing values of heat source/sink parameter and Prandtl number decreases the temperature. Also we see that the temperature is minimum at the centre of the channel (y = 0) and increasing towards the plates.

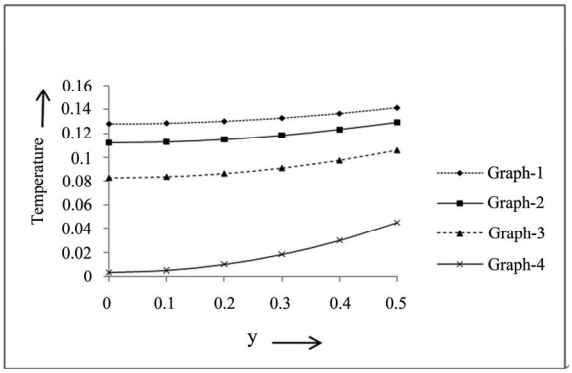

Figure 1. Temperature filed for different values of S and Pr.

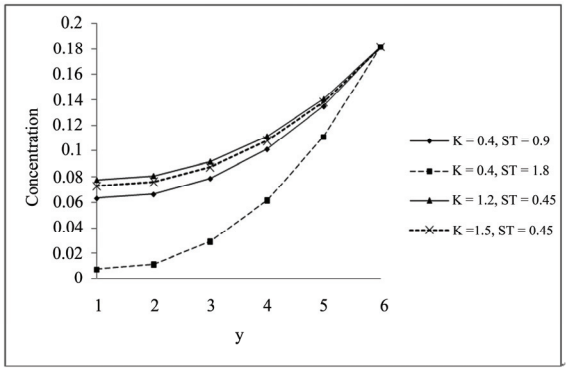

Figure 2. Concentration profile for S_T.

5.2. Concentration Profile for the Different Values of K and S_T (a = 0.2, S = 0.2,t = 1, P_r = 0.71, S_c = 0.6, D = 1)

Observation of **Figure 2** is increasing value of thermal diffusion parameter (Soret number) and chemical reaction parameter decreases the concentration. Concentration is minimum at the centre of the channel (y = 0) and increasing towards the plates.

5.3. Velocity Profile for the Different Values of K and S_T (a = 0.2, S = 0.2, t = 1, P_r = 0.71, S_c = 2, D = 1, w = 0.5, E = 1, K_1 = 10, G_m = 5, G_r = 10)

From **Figures 3 and 4** we observe that increasing value of thermal diffusion parameter (Soret number) increases the velocity of dusty fluid and dust particles while chemical reaction parameter decreases the same. Also **Figures 3 and 4** bears that the velocity is maximum at the centre of the channel and decreasing towards the plates.

5.4. Skin Friction Profile for Fluid and Dust Particles:(a = 0.2, S = 0.2, t = 1, P_r = 0.71, S_c = 2, D = 1,w = 0.5, E = 1, K_1 = 10, G_m = 5, G_r = 10)

Skin friction for different values of S_T (M = 3, K = 0.4,

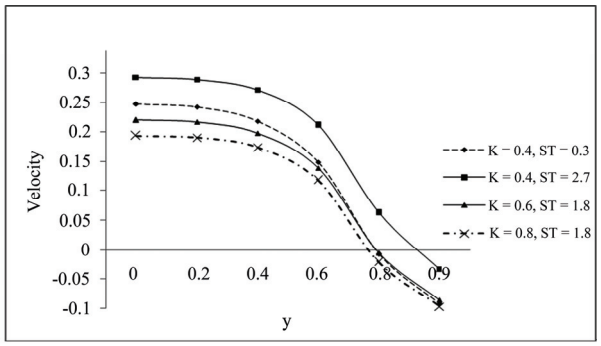

Figure 3. Velocity profile for dusty fluid.

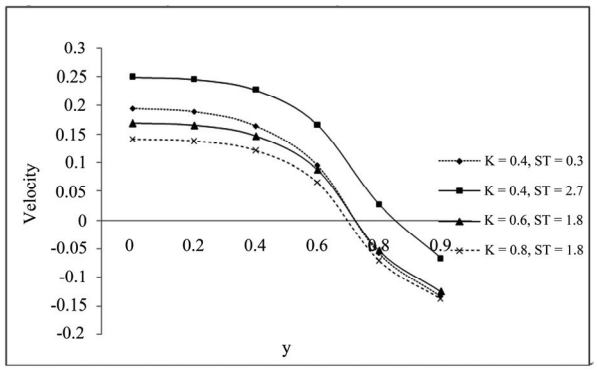

Figure 4. Velocity profile for dust particle.

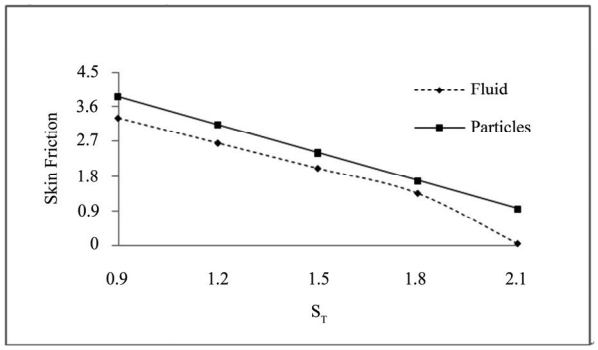

Figure 5.1. Skin friction for S_T.

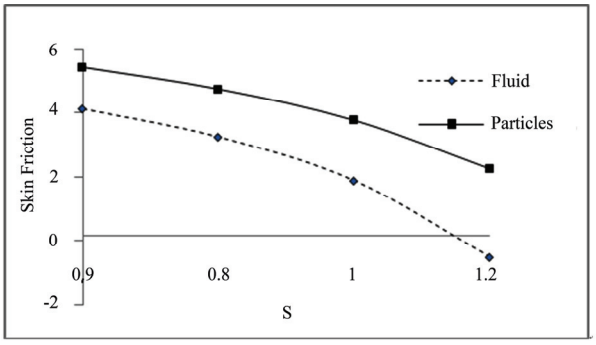

Figure 5.2. Skin friction for S.

S = 0.3):

Skin friction for different values of S, (M = 3, K = 1, S_T = 1.4):

Skin friction for different values of K (M = 3, S_T = 2.7.4, S = 0.3)**:** Skin friction for different values of M (S_T = 1.4, K = 1, S = 0.4):

The results displayed in **Figures 5.1-5.4** are as, the increasing value of thermal diffusion parameter and heat source/sink parameter decreases the skin friction of dusty fluid and dust particles. Increasing value of chemical reaction parameter and magnetic field parameter increases the skin friction of dusty fluid and dust particles.

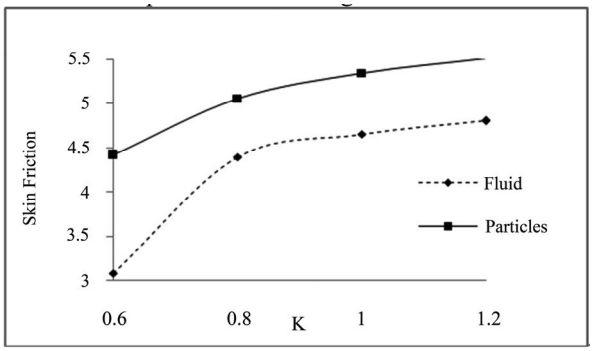

Figure 5.3. Skin friction for K.

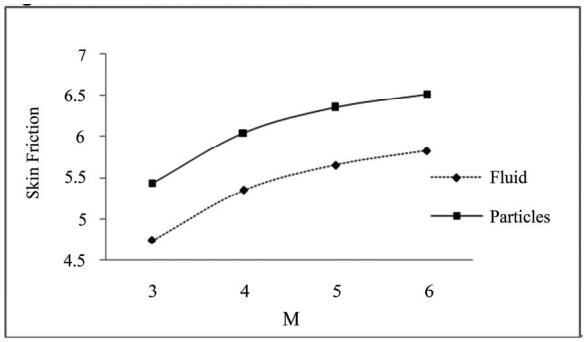

Figure 5.4. Skin friction for M.

6. Conclusions

The theoretical and numerical solutions are obtained for different profiles. From graphical representations, we have the following observations:

1) Velocity and skin friction of the dust particles behaves same as dusty fluid.

2) Increasing value of y increases the temperature, concentration while decreases the velocity of dusty fluid and dust particles.

3) Velocity of dust particles is less than velocity of dusty fluid and skin friction of dust particles is greater than that of dusty fluid.

4) Increasing values of thermal diffusion parameter (Soret number) decreases the concentration, skin friction

while increases the velocity of dust particles and dusty fluid.

5) Increasing values of magnetic field parameter increases the skin friction for both the dusty fluid and dust particles.

6) Increasing values of heat source/sink parameter decreases the skin friction for the dusty fluid as well as dust particles.

7. Acknowledgements

The author is sincerely thankful to the reviewers for the critical comments and suggestions to improve the quality of the manuscript.

REFERENCES

[1] P. L. Chambre and J. D. Young, "On Diffusion of a Chemically Reactive Species in a Laminar Boundary Layer Flow," *Physics of fluids*, Vol. 1, 1958, pp. 40-54.

[2] P. G. Saffman, "On the Stability of Laminar Flow of a Dusty Gas," *Journal of fluid mechanics*, Vol. 13, No. 1, 1962, pp. 120-129.

[3] D. H. Michael and P. W. Norey, "The Laminar Flow of a Dusty Gas between Rotating Cylinders," *The Quar- terly Journal of Mechanics and Applied Mathematics*, Vol. 21, 1968, pp. 375-388.

[4] A. Raptis and C. P. Perdikis, "Oscillatory Flow through a Porous Medium by the Presence of Free Convective Flow," *International Journal of Engineering Science*, Vol. 23, 1985, pp. 51-55.

[5] N. P. Singh, A. K. Singh, M. K. Yadav and A. K. Singh, *Acta Ciencia Indica*. Vol. XXVIII M, No. 1, 2002, pp. 089.

[6] I. U. Mbeledogu and A. Ogulu, "Heat and Mass Transfer of an Unsteady MHD Natural Convection Flow of a Rotating Fluid Past a Vertical Porous Flat Plate in the Presence of Radiative Heat Transfer," *International Journal of Heat and Mass Transfer*, Vol. 50, No. 9-10, 2007, pp. 1902-1908.

[7] P. M. Patil and P. S. Kulkarni, "Effects of Chemical Reaction on Free Convective Flow of a Polar Fluid through a Porous Medium in the Presence of Internal Heat Generation," *International Journal of Thermal Sciences*, Vol. 47, No. 8, 2008, pp. 1043-1054.

[8] E. Osalusi, J. Side and R. Harris, "Thermal Diffusion and Thermo Effect on Combined Heat and Mass Transfer of a Steady MHD Convective and Slip Flow due to a Rotating Disk with Viscous Dissipation and Ohmic Heating," *International Communications in Heat and Mass Transfer,* Vol. 35, No. 8, 2008, pp. 908-915.

[9] A. A. Afify, "Similarity Solution in MHD: Effects of Thermal Diffusion and Diffusion Thermo on Free Convective Heat and Mass Transfer over a Stretching Surface Considering Suction or Injection," *Communications in Nonlinear Science and Numerical Simulation*, Vol. 14, No. 5, 2009, pp. 2202-2214.

[10] O. A. Bég, A. Y. Bakier and V. R. Prasad, "Numerical Study of Free Convection Magnetohydrodynamic Heat and Mass Transfer from a Stretching Surface to a Saturated Porous Medium with Soret and Dufour Effects," *Computational Materials Science*, Vol. 46, No. 1, 2009, pp. 57-65.

[11] M. M. Nandeppanavar, M. S. Abel and J. Tawade, "Heat Transfer in a Walter's Liquid B Fluid over an Impermeable Stretching Sheet with Non-Uniform Heat Source/ Sink and Elastic Deformation", *Communications in Nonlinear Science and Numerical Simulation*, Vol. 15, No. 7, 2010, pp. 1791-1802.

[12] R. Sharma, R. Bhargava and P. Bhargava, "A Numerical Solution of Steady MHD Convection Heat and Mass Transfer on a Semi Infinite Vertical Porous Moving Plate Using Element Free Galerkin Method." *Computational Materials Science*, Vol. 48, No. 3, 2010, pp. 537-543.

[13] D. Kumar and R. K. Srivastava, "Effects of Chemical Reaction on MHD Flow of Dusty Visco-Elastic (Walter's Liquid model-B) Liquid with Heat Source/Sink," *Proceeding of National Seminar on Mathematics and Computer Science*, Meerut, 2005, pp. 105-112.

[14] I. Pop, *Revue Roumaine de Physiques,* Vol. 13, 1968, pp. 41.

J. Electromagnetic Analysis & Applications, 2010, 2, 588-593
doi:10.4236/jemaa.2010.210076 Published Online October 2010 (http://www.SciRP.org/journal/jemaa)

Scientific Research

A Study of Super Nonlinear Motion of Electrostatically Coupled Two-Particle System

Haiduke Sarafian

University College, The Pennsylvania State University, York, USA.
Email: has2@psu.edu

Received July 23rd, 2010; revised September 28th, 2010; accepted October 5th, 2010.

ABSTRACT

We consider a pair of nonidentical mechanical pendulums. The bob of each pendulum in addition to its own mass electrically is charged. The pendulums are hung from a common pivot in a vertical plane forming a slanted asymmetric Λ shaped figure. For arbitrary initial swings that are not necessarily confined to small angles, we analyze the dynamics of each bob under the influence of gravity's pull as well as the mutual repulsive Coulombian internal force. The equations describing the motion of the system are a set of highly, supper nonlinear coupled differential equations. Applying Mathematica we solve the equations numerically. For nonidentical parameters describing the pendulums, namely, $\{\ell, m, q, \vartheta_0\}$ *we show the system behaves chaotically; i.e. the angular position of each pendulum leaves a non-repeatable, chaotic pattern in time. For this coupled two-particle interactive system we show also by folding the time axis, the angular position of one of the pendulums vs. the other traces a Lissajous type curve. Our report includes various traditional phase diagrams and a set of newly designed, useful, phase-type diagrams as well. For a comprehensive understanding about the dynamics of the problem at hand, we provide Mathematica codes conducive to animating the chaotic motion of the system. The generic format of the codes allows adjusting the relevant parameters at will and addressing the "what-if" scenarios.*

***Keywords*:** *Nonlinear Motion, Electrostatic Interaction, Deterministic Chaotic Motion, Mathematica*

1. Introduction

In search of realistic, practical, nonlinear physics phenomena in our previous work we envision a coupled two-particle system [1,2]. In short, we consider a system composed of a pair of mechanical, electrically charged pendulums with a common pivot allowing oscillations in a vertical plane. The design of the system allows an adaptive investigation of the nonlinear oscillations. The mutual electrostatic interaction of the charged pendulums, irrespective the oscillation amplitudes make the oscillations nonlinear by itself. To make the analysis somewhat general, we consider large amplitude oscillations resulting from gravity pull and electrostatic interaction; appropriately we called the system "*super* nonlinear oscillations". For sake of transparency, however, we assume identical pendulums. Meaning, we assign the same parameters to each pendulum, such as $\{\ell,m,q\}$. Furthermore, we apply the same initial conditions such as the initial swing angles and velocities, $\{\vartheta_0, \vec{v}\}$ to both pendulums. Under these conditions, intuitively, it is plausible to conclude the pendulums are to oscillate coherently. And each pendulum is to trace a repeatable trajectory in time. And indeed we were able quantitatively confirm our intuitive predictions.

To generalize the analysis, in our current work we relax the aforementioned restrictions; we consider two nonidentical pendulums. We also select nonidentical initial conditions. Under these conditions, softly speaking, our intuition is not strong enough to predict and envision the motion of the individual pendulum.

We show, these asymmetries result unpredictable, nonrepeatable chaotic motions in time. Each pendulum under the influence of the Coulombian electrostatic force, and depending on the initial conditions traces a unique chaotic trajectory. Different initial conditions result different behavior; this is a signature of chaotic behavior. To quantify the issues of interest conducive to a better understanding of this nonlinear, chaotic system, we craft this paper as follows. In the analysis section we develop the analytic expressions describing the fundamentals of the coupled two-particle nonlinear system. In numeric section, we deploy *Mathematica* and for a host of char-

acteristic parameters and initial conditions we analyze the problem numerically; we showcase the results. To get a feel for the chaotic motion utilizing *Mathematica* animation we bring the chaotic motion of the system alive. We also display a few traditional phase diagrams. Moreover, we introduce a set of fresh, useful phase-type plots as well. We conclude the paper with a few closing remarks.

2. Analysis

Figure 1 shows the system of interest. It is composed of two asymmetric pendulums. Geometrical, mechanical, and electrical properties of each pendulum is given by the respective set of parameters, namely, $\{\ell_i, m_i, q_i, \vartheta_i\}$, with i = 1,2. The θ_i is the angular position of i^{th} pendulum from the common vertical reference. The pendulums have a common pivot and are allowed to swing in the vertical plane under the influence of the gravity and their mutual repulsive electrostatic force. The weight, tension and the electrostatic forces are designated by $\{w_i, T_i, F_{ij}\}$, for i,j = 1,2, respectively.

We consider a case where the movement of the pendulums is confined to a 2-dimansional space. **Figure 1** displays a snapshot scenario where each pendulum has assumed an angular position θ_i with respect the vertical reference. The relevant mechanical forces, namely weight and tension are depicted. We also assume the point-like particles are positively (negatively) charged, so that the mutual electrostatic force as shown is repulsive. We swing the pendulums to arbitrary initial positions to within the lower half plane and release them freely. It is the goal of our study to investigate the consequent motion of each bob.

We begin with Newton's law of motion, namely, $\vec{F}_{net} = m\vec{a}$. Applying this equation to the 2nd particle along the x and y axis yields, $(\vec{F}_{net})_{2x} = m_2 \ddot{x}_2$ and $(\vec{F}_{net})_{2y} = m_2 \ddot{y}_2$. Here over-dots indicate the second order derivative with respect to time. The x-axis equation yields,

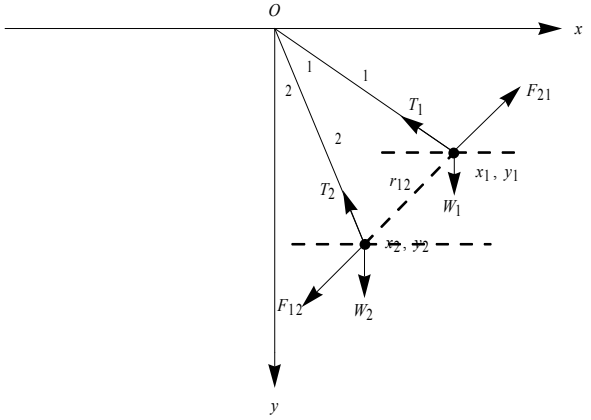

Figure 1. Display of a coupled two-particle system and their relevant mechanical and electrostatic forces.

$$-T_2 \sin\theta_2 - F_{12}\cos\phi = m_2 \ddot{x}_2 \tag{1}$$

Here the mutual electrostatic Coulomb force that particle 1 exerts on 2 is $F_{12} = \frac{\lambda}{r_{12}^2}$, where = k q_1 q_2 with k = $1/(4\pi\varepsilon_0)$ = 8.85 10^{-12} in MKS units; noting the dimension of is $[\lambda] = M L^3 T^{-2}$. The auxiliary angle shown in **Figure 1** is subject to $\cos\phi = (x_1-x_2)/r_{12}$. The abscissa of the Cartesian coordinate of the second mass can be substituted in terms of the respective angular positions; utilizing **Figure 1**, $\{x_1, x_2\} = \{\ell_1 \sin\theta_1, \ell_2 \sin\theta_2\}$. Therefore, in terms of the polar coordinates, cosφ and x-component acceleration of the second particle reads, $\cos\phi = 1/r_{12}$ $(\ell_1 \sin\theta_1 - \ell_2 \sin\theta_2)$ and $\ddot{x}_2 = \ell_2(\ddot{\theta}_2 \cos\theta_2 - \dot{\theta}_2^2 \sin\theta_2)$. Substituting these quantities in Equation (1) and rearranging the terms yields,

$$T_2 \sin\theta_2 = -\frac{\ell_1}{r_{12}^3}[\lambda(\sin\theta_1 - \frac{\ell_2}{\ell_1}\sin\theta_2) + m_2 \frac{\ell_2}{\ell_1} r_{12}^3 (\ddot{\theta}_2 \cos\theta_2 - \dot{\theta}_2^2 \sin\theta_2) \tag{2}$$

Similarly we utilize $(\vec{F}_{net})_{2y} = m_2 \ddot{y}_2$, this gives,

$$-T_2 \cos\theta_2 + F_{12}\sin\phi + m_2 g = m_2 \ddot{y}_2 \tag{3}$$

Following the steps similar the ones outlined in the previous paragraph, utilizing **Figure 1**, we write, $\{y_1, y_2\} = \{\ell_1 \cos\theta_1, \ell_2 \cos\theta_2\}$. These yields, $\sin\phi = 1/r_{12}$ $(\ell_2 \cos\theta_2 - \ell_1 \cos\theta_1)$ and $\ddot{y}_2 = -\ell_2(\ddot{\theta}_2 \sin\theta_2 + \dot{\theta}_2^2 \cos\theta_2)$. Substituting these in Equation (3) and rearranging the terms gives,

$$T_2 \cos\theta_2 = \frac{\ell_1}{r_{12}^3}[\lambda(\frac{\ell_2}{\ell_1}\cos\theta_2 - \cos\theta_1) + m_2 r_{12}^3 [\frac{g}{\ell_1} + \frac{\ell_2}{\ell_1}(\ddot{\theta}_2 \sin\theta_2 + \dot{\theta}_2^2 \cos\theta_2) \tag{4}$$

and because $\{x_1, y_1\} = \{\ell_1 \sin\theta_1, \ell_1 \cos\theta_1\}$ and $\{x_2, y_2\} = \{\ell_2 \sin\theta_2, \ell_2 \cos\theta_2\}$ the distance between the particles *i.e.* r_{12} conveniently can be written in terms of the relevant angular position angles, $r_{12} = \sqrt{(x_1-x_2)^2 + (y_1-y_2)^2} \equiv \sqrt{\ell_1^2 + \ell_2^2 - 2\ell_1\ell_2\cos(\theta_1-\theta_2)}$ Now we divide Equation (2) by Equation (4). After some tedious, laborious algebraic manipulations we arrive at,

$$\ddot{\theta}_2 + \frac{g}{\ell_2}\sin\theta_2 + \frac{\lambda}{m_2 \ell_2^3}(\frac{\ell_1}{\ell_2})\frac{\sin(\theta_1-\theta_2)}{[1+(\frac{\ell_1}{\ell_2})^2 - 2\frac{\ell_1}{\ell_2}\cos(\theta_1-\theta_2)]^{\frac{3}{2}}} = 0 \tag{5}$$

The author based on his own experience is convinced manipulating the ratio Equation (2)/Equation(4) yielding Equation (5) is more efficient manually, rather than deploying *Mathematica* symbolic manipulating utilities!

Now we apply $\vec{F}_{net} = m\vec{a}$ for particle 1. Following the steps similar to what we have already exercised for particle 2 we derive the equation describing the motion of particle 1,

$$\ddot{\theta}_1 + \frac{g}{\ell_1}\sin\theta_1 - \frac{\lambda}{m_1\ell_1^3}\left(\frac{\ell_2}{\ell_1}\right)\frac{\sin(\theta_1-\theta_2)}{\left[1+\left(\frac{\ell_2}{\ell_1}\right)^2 - 2\frac{\ell_2}{\ell_1}\cos(\theta_1-\theta_2)\right]^{\frac{3}{2}}} = 0 \quad (6)$$

The set of Equations (5) and (6) are to describe the motion of the coupled two-particle system. Each equation of the set is a second order, homogeneous and highly, *super* nonlinear ODEs. More over, these equations are coupled via a nonlinear, uneven trigonometry function, if [$\sin(\theta_1 - \theta_2)$, ℓ_1, ℓ_2, $\cos(\theta_1 - \theta_2)$]. Before we attempt solving these equations, we make a few observations. First, it is assuring to realize the lengthy algebraic manipulations of the equations yielding Equations (5,6) have the correct features. Meaning, Equation (5) yields Equation (6) for identical pendulums; *i.e.* for $\ell_1 = \ell_2$, $m_1 = m_2$ and $\theta_{01} = -\theta_{02}$. This means under these assumptions, the description of the motion of the system is given by only one equation instead of two. Moreover, this one equation is the equation we derived to describing the motion of the symmetrical pendulums in our previous work [1,2]. Second, as we discussed, the non-linearity of the motion has mechanical and electrical origins; these nonlinearities are distinctively separated in Equations (5,6). More specifically, the second and the third coefficients of Equations (5,6) are the strengths of the mechanical and electrical nonlinear terms, respectively. The coefficient of the electric nonlinear term is composed of two distinct elements; λ and the rest of the parameters. The value of λ as we defined previously is $\lambda = k\, q_1\, q_2$. Its value depends on the product of the charges. Assigning different charges to individual particle changes the overall value of the λ, however, λ contributes evenly to both equations. This is not true for the rest of the charge independent parameters. Meaning, different values of lengths and masses do contribute unevenly. Therefore, the overall value of the coefficient of the electric nonlinear term is different in Equations (5,6). Third, since the electrostatic interaction is the cause of the coupling one expects by stripping the charge(s) the equations describing the motion should reduce the one describing the oscillations of a mechanical nonlinear pendulum. For this scenario we set $\lambda = 0$; Equations (5,6) yield $\ddot{\theta}_i + \frac{g}{\ell_i}\sin\theta_i = 0$, for i = 1,2. The latter for small angle approximation *i.e.* for a linear oscillator yields the classic linearized equation of motion of a simple pendulum, $\ddot{\theta}_i + \frac{g}{\ell_i}\theta_i \sim 0$, for i = 1,2.

Now that we have confidence in the correctness of the format of the derived equations, we step forward attempting solving them. Because the equations include generic parameters describing the individual pendulum, we have the option of assigning a wide range of parameters to characterize each pendulum. For instance, one may consider two pendulums with two different lengths but the same parameters otherwise. Since the third coefficient of Equations (5,6) depends on the ratio of the lengths of the pendulums, then for instance in one scenario one may study the subsequent impact of assigning rational or irrational and real values to the ratio. Practicing one such option would open the "Pandora box". Analyzing the impact of one such scenario maybe addressed in another research project. For time being in the following section we study a subset of such options showcasing our findings.

3. Numerical Analysis

In the previous section we applied fundamentals of physics principles and developed a set of equations describing the motion of the system. These equations of motion are given with a set of coupled homogeneous highly, *super* nonlinear ODEs, namely Equations (5,6). To pin point the angular position of each bob at a given time t, one needs to solve these equations expressing angular positions as explicit functions of time, namely {θ1(t), θ2(t)}. In our first attempt to solving these equations we apply various standard symbolic methods. The *super* non-linearity of the equations come about from the electrostatic coupling term, the third terms of Equations (5,6). These are complicated trigonometric two variable functions. No wonder we fail solving these equations symbolically. We then apply *Mathematica* DSolve command; it is also unable producing any output. As a last resource we pursue solving these equations numerically. We begin with selecting a set of physically reasonable parameters describing the pendulums, such as {l,m,q}. Then we set the initial conditions, *i.e.* the initial swing angles of the pendulums. With these parameters on hand, we apply *Mathematica* NDSolve; it solves the equations. According to the aforementioned description the code reads:

In MKS units the pendulums are characterized by, values = {ℓ1→1.0, m1→8.*10^{-3}, m2→8.*10^{-3},q1→ 1.* 1.*10^{-6},q2→1.* 10^{-6},k→9 *10^{9},g→9.8};

In this example the pendulums are nonidentical; their initial swing angles are different. One is set at π/4and the other one is at 1.2 π/4.

{ℓ2,θ1init,θ2init,tmax} = {1.0,1.2 π/4,π/4,100.};

The coefficients of the second and the third terms of Equations (5,6) contain the mechanical and the electrostatic coupling parameters and are defined by {a's,b's}; {a1,b1} for the first and {a2,b2} for the second pendulum.

{{a1,b1},{a2,b2}}={{g/ℓ1,(k q1 q2)/(m1 ℓ1^3)}, {g/ℓ2,(k q1 q2)/(m2 ℓ2^3)}}/.values;

The denominators of the third terms in Equations (5) and (6) are noted by ρ21 and ρ12, respectively. Noting, ρ21=ρ12/.{ℓ1→ℓ2, ℓ2→ℓ1}

ρ21=(1+(ℓ2/ℓ1)^2-2 ℓ2/ℓ1Cos[θ1[t]-θ2[t]])/.values;

ρ12=(1+(ℓ1/ℓ2)^2-2 ℓ1/ℓ2Cos[θ1[t]-θ2[t]])/.values;

We form the ODE's given by Equations (5,6), these are,

eqnθ1=θ1"[t]+a1Sin[θ1[t]]-b1ℓ2/ℓ1Sin[θ1[t]-θ2[t]]/ $\rho_{21}^{\frac{3}{2}}$ /.values;

eqnθ2=θ2"[t]+a2Sin[θ2[t]]+b2ℓ1/ℓ2Sin[θ1[t]-θ2[t]]/ $\rho_{12}^{\frac{3}{2}}$ /.values;

Utilizing NDSolve we assume symmetrical initial conditions and drop the pendulums freely, evenly about the vertical reference through the common pivot. When invoking NDSolve, we imply the option MaxSteps →∞ otherwise for most of the cases of interest the default numeric solution routine search stops after 1000 iterations without searching the desired time span.

soleqns=NDSolve[{eqnθ1□0,eqnθ2□0,θ1[1x 10^{-8}]□θ1init,θ1'[1*10^{-8}]□0,θ2[1*10^{-8}]□θ2init,θ2'[1* 10^{-8}]□0},{θ1[t],θ2[t]},{t,1*10^{-8},tmax},MaxSteps→∞];

Utilizing the suppressed output of the numeric solutions we evaluate the kinematic quantities of interest such as, position, speed and acceleration of the individual pendulum. These set are characterized by Kinθ1 and kinθ2.

kinθ1={positionθ1,speedθ1,accθ1}=Table[D[θ1[t]/.soleqnsΠ1]],{t,n}],{n,0,2}];

kinθ2={positionθ2,speedθ2,accθ2}=Table[D[θ2[t]/.soleqnsΠ1]],{t,n}],{n,0,2}];

The next couple of lines are used to animate the motion of the swinging pendulums.

x1y1:={ℓ1Sin[θ1[t]/.soleqnsΠ1]]/.values,-ℓ1 os[θ1[t]/.soleqnsΠ1]]/.values}

x2y2:={ℓ2Sin[θ2[t]/.soleqnsΠ1]]/.values,-ℓ2 Cos[θ2[t]/.soleqnsΠ1]]/.values}

tabx1y1=Table[x1y1,{t,0,tmax,0.05}];

tabx2y2=Table[x2y2,{t,0,tmax,0.05}];

Applying Manipulate we display an alive movement of the pendulums. This helps to gain a visual understanding about how the proposed system behaves for the chosen set of parameters. The display panel includes also additional helpful diagrams such as the time series of the angular positions of the pendulums, phase profile of the pendulums, and the parametric plot of the angular position of one of the pendulums vs. the other.

Manipulate[{{Show[Graphics[{Line[{{-2,0},{2.0,0}}],Line[{{0,-2},{0,2.5}}],{Hue[0.7],Line[{{0,0},tabx1y1ΠIn]}]},{PointSize[0.025],Hue[0.0],Point[tabx1y1ΠIn]]}, {Hue[0.],Line[{{0,0},tabx2y2ΠIn]}]},{PointSize[0.025], Hue[0.],Point[tabx2y2ΠIn]]}}],ImageSize→250,PlotRange→{{-2,2},{-2,1}}],Plot[{180/πEvalate[θ1[t]/.soleqnsΠ1]],180/πEvaluate[θ2[t]/.soleqnsΠ1]]},{t,1 10^{-8},tmax-10.},AxesLabel→{"t,s","θ1,θ2"},PlotStyle→{Blue,Red}]},{ParametricPlot[Flaten[{kinθ2Π1]],kinθ2Π2]]}],{t,1*10^{-8},tmax-50},AxesLabel→{" θ_2 "," θ_2 "},AspectRatio→1,PlotRange→All,PlotStyle→Red],

ParametricPlot[Flatten[{kinθ1Π1]],kinθ1Π2]]}],{t,1* 10^{-8},tmax-50.},AxesLabel→{" θ_1 "," θ_1 "},AspectRatio→1,PlotRange→All,PlotStyle→Blue],

ParametricPlot[Flatten[{kinθ1Π1]],kinθ2Π1]]}],{t,1* 10^{-8},tmax-50},AxesLabel→{"θ1","θ2"},AspectRatio→1, PlotRange→All,PlotStyle→Black]

}

},{{n,1,"frame"}, 1,Length[tabx1y1],1}]

To show the impact of the initial conditions on the behavior of the system, in **Figure 4** we display plots similar the one shown in **Figure 3**. The only difference parameterizing the system is the initial swing angle of the left side pendulum; it is set at $\theta_{02} = -1.2\pi/4$. For instance the phase profile of the first pendulum displaced by the first graphs of the **Figures 3,4** are quite distinguishable. Also the difference between the left lower graphs, the parametric plots of the angular position of the second pendulum vs. the first one is drastic. These very much resemble the Lissajous curves.

Note, a classic Lissajous curve is referred to a closed curve that is being traced by *one* particle subject to simultaneous harmonic motions in two perpendicular directions. In our study the Lissajous curves are traced by combining the oscillations of *two* particles subject to oscillations with a relative arbitrary phase difference.

Reviewing **Figures 2-7** reveals for the chosen set of initial conditions the motion of the each pendulum is chaotically deterministic. That is to say there should be a relation such as $\theta_{i,n+1} = f_i(\theta_i, n)$ for i = 1,2. Where θi,n is the angular position of one of the pendulums at a sampled time and f is the mapping procedure. In its simplest form we explore the existence of one such possibility following procedure outlined in [3] *i.e.* we plot θi,n+1 vs. θi,n, these are shown in **Figure 8**. According to these plots and according to our speculations, indeed the time series depicted in **Figure 2**, are not noise, rather underline a deterministic chaotic behavior. Interested reader utilizing the embedded code may explore similar plots for various possible characteristic parameters some have

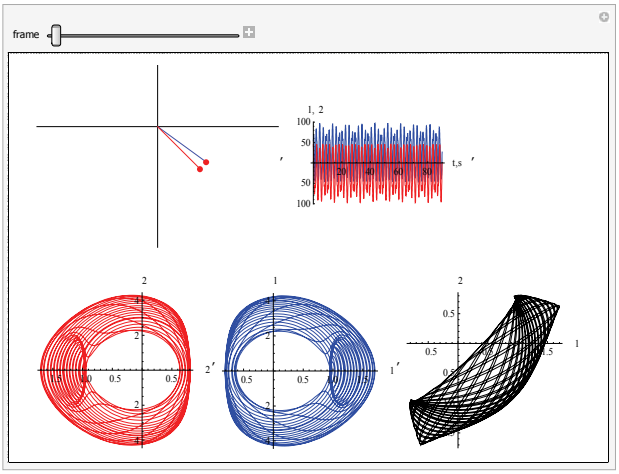

Figure 2. Top row from left to right: a snapshot of the animation, the time series of the pendulums. Second row: the phase profile of the left (Red) and the right (Blue) pendulums, the parametric plot of the angular positions of the second pendulum vs. the first.

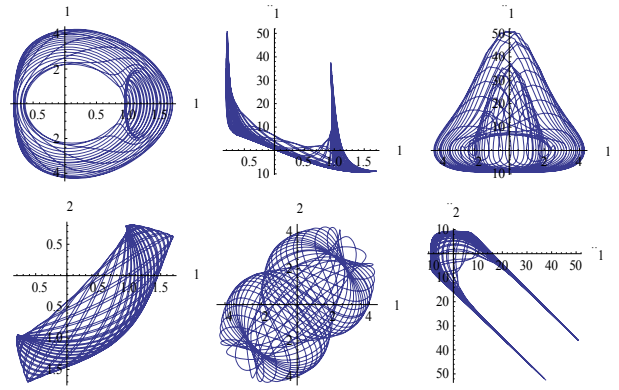

Figure 3. An extended graphic version of the plots of Figure 2. The second and third plots of the first and the second row are fresh additions to our classic/traditional plots.

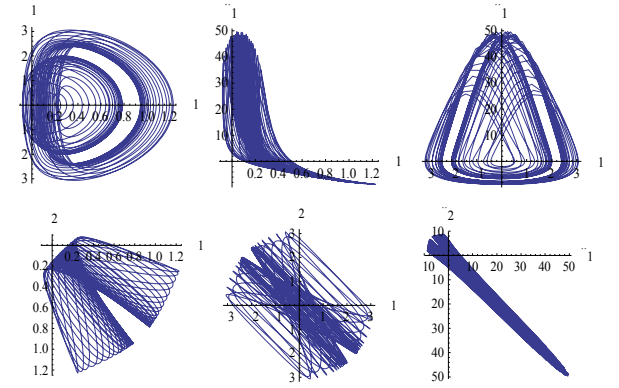

Figure 4. The impact of the initial angle on the characteristic behavior of the system. The initial angle for the left particle is set at $\theta_{01} = -1.2\pi / 4$.

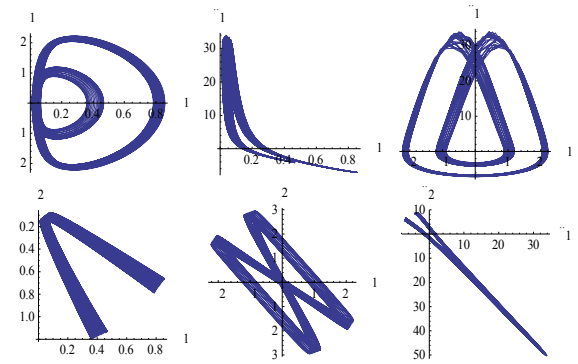

Figure 5. Same as Figure 4, with the exception of instead of identical masses we assumed $m_1 = 12/8\ m_2$.

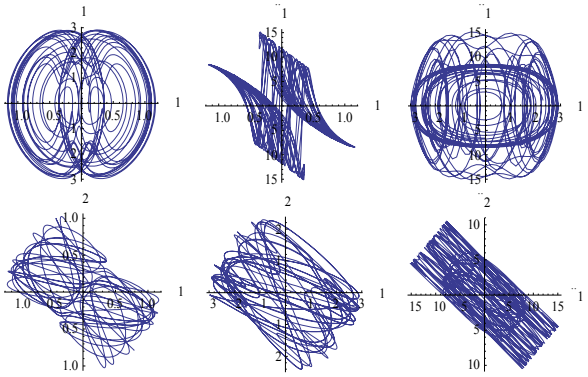

Figure 6. Same as Figure 4, with the exception of the length of the left side pendulum is $\ell_2 = 1.2\ell_1$.

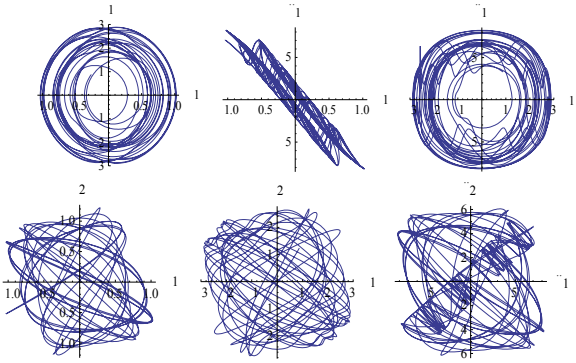

Figure 7. Two totally different pendulums with different initial conditions: $\ell_2 = 1.4\ell_1$, $\theta_{02} = -1.2\theta_{01}$, $m_1 = 12/8 m_2$.

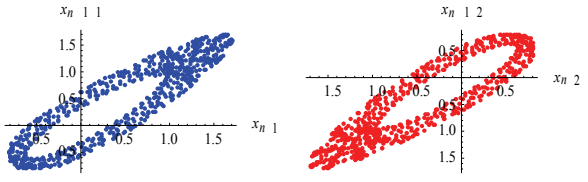

Figure 8. Plots of $\theta_{i,n+1}$ vs. $\theta_{i,n}$ for i = 1,2. The left graph depicts the first pendulum and the right graph shows the second pendulum. Parameters are as the same used in Figure 2.

been discussed in the text.

```
tabθ1=Table[{N[t],θ1[t]/.soleqnsΠ1]]},{t,1*10^-8,tmax,
0.15}];
tabθ2=Table[{N[t],θ2[t]/.soleqnsΠ1]]},{t,1*
10^-8,tmax,0.15}];
tabθ1n=Table[tabθ1Πn,2]],{n,Length[tabθ1]-1}];
tabθ2n=Table[tabθ2Πn,2]],{n,Length[tabθ2]-1}];
tabθ1nplus1=Table[tabθ1Πn+1,2]],{n,Length[tabθ1]-
1}];
tabθ2nplus1=Table[tabθ2Πn+1,2]],{n,Length[tabθ2]-
1}];
transposeNNplus1=Transpose[{tabθ1n,tabθ1nplus1}];
transposeNNplus2=Transpose[{tabθ2n,tabθ2nplus1}];
s1=ListPlot[transposeNNplus1,PlotStyle→{Blue},Plot
Range→All,AxesLabel→{"(x_n)_1","(x_n+1)_1"}];
s2=ListPlot[transposeNNplus2,PlotStyle→{Red},Plot
Range→All,AxesLabel→{"(x_n)_2","(x_n+1)_2"}];
GraphicsArray[{s1,s2},ImageSize→400]
```

4. Conclusions

It is the objective of our analysis to explore real-life cases conducive to nonlinear physical phenomena. We suggest a system composed of a pair of charged pendulums that are free to oscillate in a vertical plane under the gravity pull and mutual electrostatic interaction. In addition to the large angle oscillations which by itself is a source of nonlinear oscillations we include the electrostatic interaction. As we show, the latter contributes strongly to the non-linearity of the oscillations. We formulate the problem at hand symbolically for a general case. The system under the consideration describes a general setting of its kind. This is a major modification vs. our previous work where only symmetrical, identical pendulums were considered. Applying *Mathematica* we analyze the problem numerically. From this analysis we gain a valuable insight about the chaotic motion. For a comprehensive understanding we showcase our findings. We conclude the paper pointing to the deterministic chaotic behaviors of the system. The plot of angular position of one of the pendulums vs. the other traces a Lissajous type curve. We show the chaotic behavior of the system underlines an attractor. The paper includes a series of *Mathematica* codes assisting the interested reader to investigate the problem further.

REFERENCES

[1] H. Sarafian, "A Study of Super Nonlinear Motion of a Simple Pendulum," *The Mathematica Journal*, Vol. 11, in press.

[2] H. Sarafian, "A Study of Super Nonlinear Motion of a Simple Pendulum and Its Generalization," *International Conference on Computational Science and Its Applications*, Yongin, 2009, pp. 97-103.

[3] F. Takens, "Detecting Strange Attractors in Turbulence," In: D. A. Rand and L. S. Young, Eds., *Lecture Notes in Mathematics*, Springer-Verlag, New York, 1981.

J. Electromagnetic Analysis & Applications, 2010, 2, 594-597
doi:10.4236/jemaa.2010.210077 Published Online October 2010 (http://www.SciRP.org/journal/jemaa)

Detection of Blood Traces in Human Pericardial Fluid Using Microwaves

Anil Lonappan

Department of Electrical Engineering, Mangosuthu University of Technology, Durban, South Africa.
Email: lonappan@mut.ac.za

Received August 12th, 2010; revised September 1st, 2010; accepted September 25th, 2010.

ABSTRACT

This communication reports a novel method of analyzing pericardial fluid and finding blood traces present based on the measurement of the dielectric properties at microwave frequencies. The experiment was performed by cavity perturbation method in the S-band of microwave frequency with the pericardial fluid from healthy persons as well as from patients suffering from pericardial bleeding. It is noted that considerable variation in the dielectric properties of patient samples with the normal healthy samples and these measurements were in good agreement with clinical analysis. This measurement technique and the method of extraction of pericardial fluid are simple and both are non invasive. These results give light to an alternative in-vitro method of diagnosing onset pericardial bleeding abnormalities using microwaves without surgical procedure.

***Keywords*:** *Pericardial Fluid, Pericardial Bleeding, Cavity Perturbation, Clinical Analysis*

1. Introduction

The survival rate is increased in heart patients based on the earlier detection of heart abnormalities or rhythm. Numerous diagnostic techniques are available for detecting heart abnormalities and most of the techniques are either invasive or noninvasive and most of them are time consuming procedures. These concerns augment the search for new techniques that can find other physical tissue properties at the onset of heart abnormalities.

Pericardial fluid is secreted by the serous membrane on the pericardious sac on the outside of the heart. The pericardial cavity contains between 15 and 50ml of pericardial fluid. It is similar to the serous fluid that is found in the brain for cushioning and ability to move semi-freely. In pericardial bleeding there is the presence of pericardial fluid with blood and is an abnormal condition and there will be accumulation of fluid in the pericardial cavity. Because of the limited amount of space in the pericardial cavity, this fluid accumulation will lead to an increased intrapericardial pressure and can negatively affect heart function. When there is a pericardial bleeding with enough pressure to adversely affect heart function, this is called cardiac tamponade. While small bleeding occur in many clinical scenarios and are not necessarily dangerous, large and rapidly accumulating bleeding may cause cardiac tamponade, a life-threatening complication. Ben-Horin *et al.* studied the composition of pericardial fluid in patients undergoing open heart surgery [1]. Diagnosing the onset pericardial bleeding abnormalities are crucial to increase the survival rate and the present study reports a new method of detecting the onset of pericardial bleeding based on the measurement of the dielectric properties of pericardial fluid using cavity perturbation technique in the S-band of microwave frequencies.

Medical science has advanced greatly in the last century, there is still much that is not understood about the way the human body interacts with many things, including microwaves. The potential for medical uses of microwaves lies in two areas therapeutic and diagnostic field and many new medical microwave devices are also developed [2,3]. All the known therapeutic uses of microwaves involve the heating of tissue. Carefully controlled, microwave-generated heat can have a therapeutic effect on a number of ailments. Microwave medical devices ability depends upon how far microwaves can deeply penetrate into living tissues. The depth to which microwaves can penetrate tissues is primarily a function of the dielectric properties of tissues and of the frequency of the microwaves. Lower the water content of the tissue the deeper a wave at a given frequency and lower the frequency the deeper is the depth of penetration into tissues with given water content. Thus, there is a need to

study the interaction of microwave with tissues especially its effect on biological materials. The key element in the microwave study is the determination of the absorbed energy. The amount of energy absorbed is a function of the complex permittivity of a material [4]. Hence, it is crucial to know the dielectric properties of biological materials and the various constituents thereof. Exhaustive studies of dielectric parameters of various human tissues and body fluids at different RF frequencies have been reported [5-7]. Different measurement techniques are used to measure the complex permittivity of a material and the chosen technique depends on various factors such as the nature of the sample and the frequency range used [8-11]. When only very small volumes of the sample are available, the cavity perturbation technique is an attractive option as it requires only minute volumes for the measurement [12]. This makes it suitable for the dielectric study of pericardial fluid, as only very small volumes can be only be extracted by procedure. The rectangular cavity perturbation technique has been employed for the measurement of the dielectric parameters of pericardial fluid samples obtained from healthy persons as well as from patients with pericardial bleeding in this work, in the frequency range 2 to 3 GHz. It is noticed that a remarkable change in the dielectric properties of bleeding samples with the normal healthy samples and these measurements were in good agreement with clinical analysis. This microwave measurement procedure is simple and extraction of pericardial fluid from persons is least painful and nonsurgical in nature. These results prove an alternative in-vitro method of detecting the onset of pericardial bleeding based on the measurement of the dielectric properties of pericardial fluid using microwaves without surgical procedure.

2. Sample Preparation

The skin of the chest will be cleaned with antibacterial soap and a small needle is inserted into the chest between the ribs into the pericardium, which is the thin sac that surrounds the heart, and a small amount of fluid is withdrawn. Then the samples were filled in the sample holder and kept at 1°C. Measurements were carried out on samples which were less than one day old.

3. Material and Methods

The experimental set-up consists of a transmission type S-band rectangular cavity resonator, HP 8714 ET network analyser. The cavity resonator is a transmission line with one or both ends closed. The numbers of resonant frequencies are determined by the length of the resonator. The resonator in this set-up is excited in the $TE_{10\rho}$ mode. The sample holder which is made of glass in the form of a capillary tube flared to a disk shaped bulb at the bottom is placed into the cavity through the non-radiating cavity slot, at broader side of the cavity which can facilitate the easy movement of the holder. The resonant frequency f_o and the corresponding quality factor Q_o of the cavity at each resonant peak with the empty sample holder placed at the maximum electric field are noted. The same holder filled with known amount of sample under study is again introduced into the cavity resonator through the non-radiating slot. The resonant frequency of the sample loaded cavity is selected and the position of the sample is adjusted for maximum perturbation (*i.e.* maximum shift of resonant frequency with minimum amplitude for the peak). The new resonant frequency f_s and the quality factor Q_s are noted. The same procedure is repeated for other resonant frequencies.

4. Theory

When a material is introduced into a resonant cavity, the cavity field distribution and resonant frequency are changed which depend on shape, electromagnetic properties and its position in the fields of the cavity. Dielectric material interacts only with electric field in the cavity

According to the theory of cavity perturbation, the complex frequency shift is related as [12]

$$-\frac{d\Omega}{\Omega} \approx \frac{(\bar{\varepsilon}_r - 1)\int_{V_s} E.E_0^* dV}{2\int_{V_c}\left|E_0\right|^2 dV} \quad (1)$$

$$\text{But } \frac{d\Omega}{\Omega} \approx \frac{d\omega}{\omega} + \frac{j}{2}\left[\frac{1}{Q_s} - \frac{1}{Q_0}\right] \quad (2)$$

Equation (1) and (2) and separating real and imaginary parts results

$$\varepsilon_r^{/} - 1 = \frac{f_o - f_s}{2f_s}\left(\frac{V_c}{V_s}\right) \quad (3)$$

$$\varepsilon_r^{//} = \frac{V_c}{4V_s}\left(\frac{Q_o - Q_s}{Q_o Q_s}\right) \quad (4)$$

Here, $\bar{\varepsilon}_r = \varepsilon_r^{/} - j\varepsilon_r^{//}$, $\bar{\varepsilon}_r$ is the relative complex permittivity of the sample, $\varepsilon_r^{/}$ is the real part of the relative complex permittivity, which is known as dielectric constant. $\varepsilon_r^{//}$ is the imaginary part of the relative complex permittivity associated with the dielectric loss of the material. V_s and V_c are corresponding volumes of the sample and the cavity resonator. The conductivity can be related to the imaginary part of the complex dielectric constant as:

$$\sigma_e = \omega\varepsilon'' = 2\pi f \varepsilon_0 \varepsilon_r'' \quad (5)$$

5. Results and Discussions

The microwave studies of pericardial fluid samples were done using cavity perturbation technique collected from healthy donors as well as from the patients and the results are shown in **Figures 1,2**. These results are novel using microwave techniques for the case of pericardial fluid. Clinical evaluation of the pericardial fluid samples is also done and the results are tabulated in **Table 1**. They found it was relatively rich in lactate dehydrogenase, low in protein and high in lymphocytes and monocytes. From **Figure 1** it is noticed that the bleeeding samples exhibit a higher dielectric constant than that of the normal samples. In **Figure 2** the variation of conductivity of normal and bleeding samples are plotted. It can be found that distinct variation in the conductivities of normal samples and the bleeding samples. The increase in conductivity in bleeding samples is due to the presence of higher level of protein contents such as albumin and globulin as well as blood traces. Thus in the specified band of frequencies, normal pericardial and pericardial bleeding samples were studied and exhibit distinct variation of dielectric constant and conductivity with frequency.

Table 1. Variation of constituents in normal pericardial fluid samples as well as pericardial bleeding samples.

Sample	Colour	Lactate Dehydrogenase (10^3/mm^3)	Lyphocytes(10^3/mm^3)	Mocytes (10^3/mm^3)	Proteins(gm/dL)	
					Albumin	Globulin
PN-1	Clear	2.2	0.5	1.4	3.5	3.4
PN-2	Clear	1.9	0.4	1.2	4.2	2.9
PN-3	Cloudy	2.6	0.6	1.5	3.8	3.1
PN-4	Clear	2.1	0.5	1.3	4.9	2.3
PE-5	Bloody	2.2	1.8	4.3	13.9	14.1
PE-6	Bloody	2.1	1.9	4.0	12.8	10.3
PE-7	Bloody	2.7	1.3	3.9	16.2	13.4
PE-8	Bloody	3.1	1.4	4.2	14.4	15.6

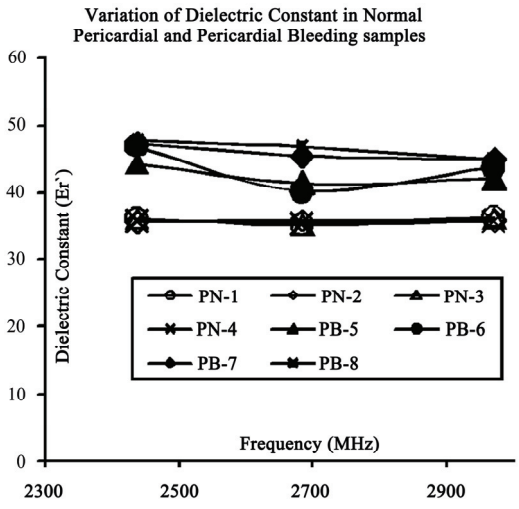

Figure 1. Variation of dielectric constant in normal pericardial sample and pericardial bleeding samples.

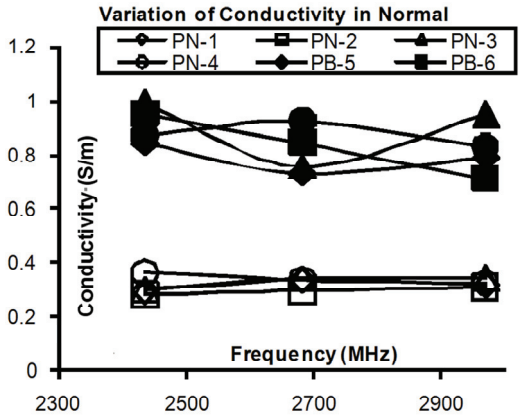

Figure 2. Variation of conductivities in normal pericardial sample and pericardial bleeding samples.

6. Conclusions

The microwave characterisation of the pericardial samples is done using cavity perturbation technique. The cavity perturbation technique is quick, simple, and accurate and it requires very low volume of sample for measuring the dielectric properties of tissue samples like pericardial samples. It is observed that a remarkable change in the dielectric properties of pericardial bleeding samples with the normal healthy samples and these measurements were in good agreement with clinical analysis. This measurement technique is simple and the extraction of pericardial fluid from persons is least painful and nonsurgical in nature. These results prove an alternative in-vitro method of diagnosing onset pericardial bleeding abnormalities using microwaves without surgical procedure.

REFERENCES

[1] S. Ben Horin, A. Shinfeld, E. Kachel, A. Chetrit and A. Livneh, "The Composition of Normal Pericardial Fluid and Its Implications for Diagnosing Pericardial Effusions," *American Journal of Medicine*, Vol. 118, No. 6, 2005, pp. 636-640.

[2] A. Rosen and H. D. Rosen, "New Frontiers in Medical Device Technology," Wiley, New York, 1995.

[3] "Mini-Special Issue on RF/Microwave Applications in Medicine," IEEE Transactions on Microwave Theory Technique, Vol. 48, 2000.

[4] A. Von Hippel, "Dielectric and Waves," Artech House, 1995.

[5] S. Gabriel, R. W. Lau and C. Gabriel, "The Dielectric

Properties of Biological Tissues: II. Measurements on the Frequency Range 10Hz to 20GHz," *Literature Survey, Physics Medicine Biology*, Vol. 41, No. 11, 1996, pp. 2251-2269.

[6] H. F. Cook, "Dielectric Behavior of Human Blood at Microwave Frequencies," *Nature*, Vol. 168, 1951, pp 247-248.

[7] H. F. Cook, "The Dielectric Behavior of Some Types of Human Tissues at Microwave Frequencies," *British Journal of Applied Physics*, Vol. 2, 1951, pp 295-300.

[8] D. K. Ghodgaonkar, V. V. Varadan and V. K. Varadan, "Free Space Measurement of Complex Permittivity and Complex Permeability of Magnetic Materials at Micro-Wave Frequencies," *IEEE Transactions on Instrumentation and Measuremen*t, Vol. 19, 1990, pp. 387-394.

[9] D. K Ghodgaonkar, V. V. Varadan and V. K. Varadan, "A Free Space Method for Measurement ff Dielectric Constant and Loss Tangents at Microwave Frequencies," *IEEE Transaction on Instrumentation and Measurement*, Vol. 38, 1989, pp. 789-793.

[10] W. Barry, "A Broadband, Automated, Stripline Technique for the Simultaneous Measurement of Complex Permittivity and Complex Permeability," *IEEE Transaction on Microwave Theory and Techniques*, Vol. 34, 1986, pp. 80-84.

[11] Z. Abbas, R. D. Pollard and R. W. Kelsall, "A Rectangular Dielectric Waveguide Technique for Determination of Permittivity of Materials at W-Band," *IEEE Transactions on Microwave Theory and Techniques*, Vol. 46, 1998, pp 2011-2015.

[12] K. T. Mathew, "Perturbation Theory," *Encyclopedia of RF and Microwave Engineering*, Vol. 4, 2005, pp. 3725-3735.

J. Electromagnetic Analysis & Applications, 2010, 2, 598-600
doi:10.4236/jemaa.2010.210078 Published Online October 2010 (http://www.SciRP.org/journal/jemaa)

Synthesis, Morphology and Magnetic Characterization of Zn Ferrite Powders

Simona Alexandra Popescu[1], Paulina Vlazan[1], Petru V. Notingher[2], Stefan Novaconi[1], Ioan Grozescu[1], Alexandra Bucur[1], Paula Sfirloaga[1]

[1]National Institute for Research and Development in Electrochemistry and Condensed Matter, Timisoara, Romania; [2]Politehnica University of Bucharest, Electrical Engineering Faculty, Bucharest, Romania.
Email: simona2008@gmail.com

Received September 3rd, 2010; revised September 27th, 2010; accepted October 3rd, 2010.

ABSTRACT

We synthesized $Zn_{0.8}Fe_{2.2}O_4$ ferrite powders by coprecipitation and hydrothermal techniques and analyzed the morphology and magnetic properties. The morphology and structure of the Zn ferrite powders were investigated using Scanning Electron Microscopy (SEM) and X-ray Diffraction (XRD) identifying the crystallization planes. Magnetic hysteresis curves were obtained for the Zn ferrites samples.

***Keywords*:** *Zn Ferrites, Hysteresis, Morphology and Structure*

1. Introduction

Ferrite nanopowders have scientific and technological importance in recent years due to their magnetic properties and have a broad range of applications such as magnetic recording, ferrofluids, magnetic resonance imaging, biomedicine, catalyst, etc. [1,2]. They have been used for high-frequency transformers cores, rod antennas, radio frequency coils and more recently as radar-absorbing materials [3,4]. Spinel ferrites are materials with good magnetic and electronic properties, which depend strongly on the cation distribution among the tetrahedral and octahedral sites [5]. Ferrite materials can also absorb electromagnetic radiation in the microwave bands when cast in various forms, e.g., sheets, paints, films, ceramic tiles, powders, and loads in matrix composites or mixed with a conducting material [6-11]. Among the spinel ferrites, Zn ferrites are utilized as electromagnetic wave absorbing materials [12,13].

In this work we analyzed the morphological and magnetic properties of $Zn_{0.8}Fe_{2.2}O_4$ powders synthesized by the coprecipitation and hydrothermal techniques.

2. Experimental Procedure

The $Zn_{0.8}Fe_{2.2}O_4$ ferrite powders were prepared by coprecipitation (sample S1 in **Figure 1(a)**) and hydrothermal technique (sample S2 in **Figure 1(b)**) using iron nitrate, zinc nitrate and sodium hydroxide as reaction agents.

To obtain $Zn_{0.8}Fe_{2.2}O_4$ ferrite powders using the coprecipitation method we have mixed iron nitrate, zinc nitrate and sodium hydroxide with bidistilled water. The solution was heated to 90°C during 5 hours on a Magnetic Agitator at 400 rpm. To obtain the final zinc ferrite powder the solution was then cleaned with bidistilled water and alchool, filtered for 5 hours for neutral pH and calcinated in a Nabertherm Oven at 200°C for 2 hours.

Using the hydrothermal method for synthesing zinc ferrite we combined iron nitrate and zinc nitrate with bidistilled water and sodium hydroxide and introduced it in an autoclave for 5 hours at 200°C in an Heraeus 6060 UT Stove. To obtain the zinc powder the final solution was cleaned and filtered with bidistilled water for 5 hours to obtain neutral pH and then dried.

3. Morphology and Structure Characterization

3.1. SEM Analysis

Performing Scanning Electron Microscopy (SEM) with an FEI Company microscope, type Inspect S we analyzed the structure of $Zn_{0.8}Fe_{2.2}O_4$ powder and show typical micrographs in **Figures 1(a),1(b)**. For the sample S1 shown in **Figure 1(a)** syntesized by the coprecipitation method the surface has compacted shapes with round particles, while for sample S2 shown in **Figure 1(b)** obtained by the hydrothermal method the particles exhibit elongated shapes. For both samples the micrographs ex-

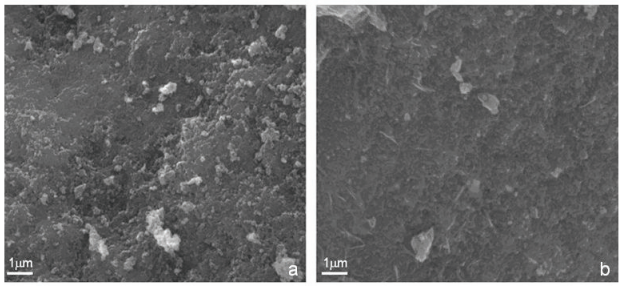

Figure 1. SEM micrographs of $Zn_{0.8}Fe_{2.2}O_4$ powders for sample S1—coprecipitation (a) and sample S2—hydrothermal (b).

hibit compact structures with smallest particles sizes typically less than 100 nm. Thus we observed structural differences in the aggregation of the material for the two synthesis techniques.

3.2. XRD Analysis

Figure 2 shows typical X-ray diffraction patterns of $Zn_{0.8}Fe_{2.2}O_4$ powder analysed with a Philips difractometer, type X'Pert PRO MPD.

The measurements were done in the 2θ range of 20°-90° for samples of zinc ferrites obtained by the two techniques. The calculated distance between the main crystal planes was 0.2 nm. Well defined diffraction peaks corresponding to the characteristic planes (311), (511) and (440) apear at 35°, 57° and 64°. The intensity of the peaks reveal that the sample S2 obtained by the hydrothemal method has bigger particles then the sample S1 obtained by coprecipitation. Other wide diffraction peaks corresponding to (220), (442), (553) and (731) planes are also present with low relative intensities asumed to arise from an amorphous structure. Using the Scherrer Equation [14], the measured size of zinc ferrites particles was bellow 100 nm.

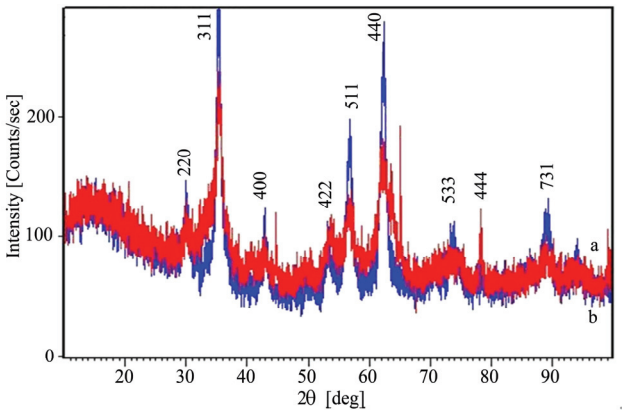

Figure 2. XRD graphs of $Zn_{0.8}Fe_{2.2}O_4$ obtained by two synthesis methods for sample θ S1—coprecipitation (a) and sample S2—hydrothermal (b).

4. Magnetic Hysteresis Measurements

We analyzed the magnetic behavior of the zinc ferrite obtained by coprecipitation and hydrothermal methods by measuring the magnetization as a function of an applied 50 Hz, AC magnetic field amplitude up to 160 kA/m [15].

In **Figures 3(a),3(b)** the M-H curves of the sample S1 and S2 obtained by the two synthesis methods are given.

In the case of the sample S1 obtained by coprecipitation a superparamagnetic-like behavior was observed, with a maximum magnetization of 200 A/m at 160 kA/m. The maximum magnetization of the sample S2 obtained by the hydrothermal method is 750 A/m for a maximum applied field of 160 kA/m, the magnetic remanence was 70 A/m and coercivity about 6.40 kA/m.

5. Discussion

The analysis of the morphology and structure by electron microscopy for zinc ferrites shows that the powders are composed of particles with diameters bellow 100 nm for both S1—coprecipitation and S2—hydrothermal samples. From the x-ray diffraction measurements we observe for both synthesis methods the crystal planes (311), (511)

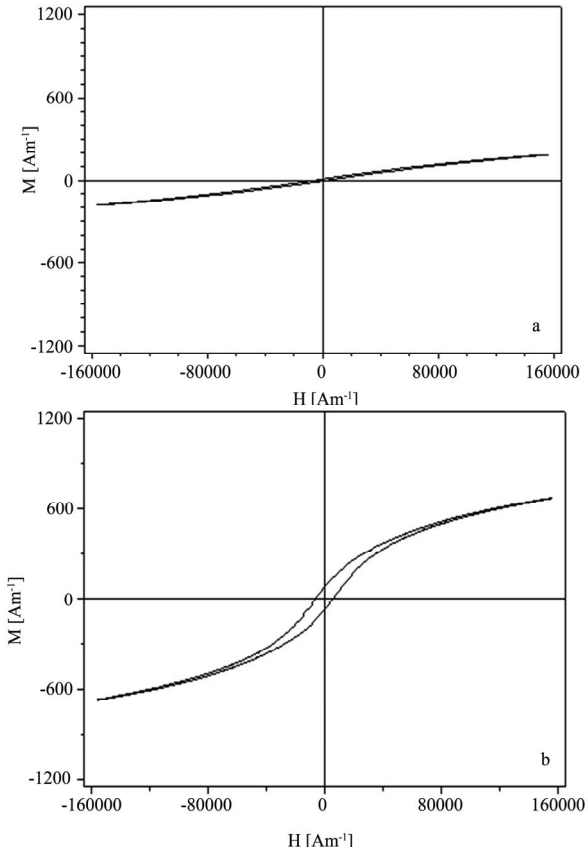

Figure 3. Hysteresis curves of the $Zn_{0.8}Fe_{2.2}O_4$ powders for sample S1—coprecipitation (a) and S2—hydrothermal (b).

and (440) though the intensity of the peaks of the zinc ferrite obtained by the hydrothermal method gave bigger particles by about 10% as compared to the coprecipitation method. These diffraction peaks correspond to the main diffraction planes in zinc ferrites although some amorphous material structure is observed also by the wide and small peaks of planes (220), (442), (553) and (731). We also observed that the structure for the sample S2—hydrothermal is more crystalline while for the sample S1—coprecipitation the surface structure is more homogenous.

From the hysteresis measurements the $Zn_{0.8}Fe_{2.2}O_4$ powders obtained in this investigation we obtained a ferromagnetic behavior [16] with stronger hysteresis for the sample S2—hydrothermal wich means that they can be stronger magnetized.

6. Conclusions

Two synthesis methods were investigated to obtain the zinc ferrites with magnetic properties usable for shielding applications.

The zinc ferrite nanopowder synthesized by the hydrothermal technique shows a higher magnetic behavior as seen from the hysteresis curves. From x-ray diffraction measurements the zinc ferrite particles for sample S2—hydrothermal have bigger sizes compared to the samples S1—coprecipitation. The ferrite nanopowder obtained by both methods show small particles with diameters typically bellow 100 nm resting on a more planar structure.

We conclude that the synthesis method has important influence on the morphology, structure and magnetic behavior of the zinc ferrite nanopowders and in our case the hydrothermal method gave superior magnetic results.

REFERENCES

[1] H. Montiel, G. Alvarez, M. P. Gutiérrez, R. Zamorano and R. Valenzuela, "Microwave Absorption in Ni–Zn Ferrites through the Curie Transition," *Journal of Alloys and Compound*, Vol. 369, 2004, pp. 141-143.

[2] H. W. Wang and S. C. Kung, "Crystallization of Nanosized Ni-Zn Ferrite Powders Prepared by Hydrothermal Method," J*ournal of Magnetism and Magnetic Materials*, Vol. 270, 2004, pp. 230-236.

[3] A. M. Kumar, M. C. Varma, C. L. Dube, K. H. Rao and S. C. Kashyap, "Development of Ni–Zn Nanoferrite Core Material with Improved Saturation Magnetization and DC Resistivity," *Journal of Magnetism and Magnetic Materials*, Vol. 320, 2008, pp. 1995-2000.

[4] Y. Hwang, "Microwave Absorbing Properties of NiZn-Ferrite Synthesized from Waste Iron Oxide Catalyst," *Materials Letters*, Vol. 60, 2006, pp. 3277-3280.

[5] M. Wen, Q. Li and Y. Li, "Magnetic, Electronic and Structural Properties of $Zn_xFe_{3-x}O_4$," *Journal of Electron Spectroscopy and Related Phenomena*, Vol. 153, 2006, pp. 65-70.

[6] M. Koledintseva, J. Drewniak, Y. Zhang, J. Lenn and M. Thoms, "Modeling of Ferrite-Based Materials for Shielding Enclosures," *Journal of Magnetism and Magnetic Materials*, Vol. 321, 2009, pp. 730-733.

[7] M. Sivakumar, A. Towata, K. Yasui, T. Tuziuti and Y. Iida, "A New Ultrasonic Cavitation Approach for the Synthesis of Zinc Ferrite Nanocrystals," *Current Applied Physics*, Vol. 6, 2006, pp. 591-593.

[8] A. D. Sheikh and V. L. Mathe, "Anomalous Electrical Properties of Nanocrystalline Ni–Zn Ferrite," *Journal of Material Science*, Vol. 43, 2008, pp. 2018-2025.

[9] K. Kondo, T. Chiba, H. Ono, S. Yoshida, Y. Shimada, N. Matsushita and M. Abe, "Conducted Noise Suppression Up to GHz Range by Spin-Sprayed $Ni_{0.2}Zn_xFe_{2.8-x}O_4$ (x = 0.3, 0.6) Films Having Different Natural Resonance Frequencies," *Journal of Magnetism and Magnetic Materials*, Vol. 301, 2006, pp. 107-111.

[10] A. C. F. M. Costa, E. Tortella, M. R. Morelli, M. Kaufman and R. H. G. A. Kiminami, "Effect of Heating Conditions during Combustion Synthesis on the Characteristics of $Ni_{0.5}Zn_{0.5}Fe_2O_4$ Nanopowders," *Journal of Material Science*, Vol. 37, 2002, pp. 3569-3572.

[11] L. Chen, Y. Shen and J. Bai, "Large-Scale Synthesis of Uniform Spinel Ferrite Nanoparticles from Hydrothermal Decomposition of Trinuclear Heterometallic Oxo-Centered Acetate Clusters," *Materials Letters*, Vol. 63, 2009, pp. 1099-1101.

[12] A. Rafferty, Y. Gunko and R. Raghavendra, "An Investigation of Co-Fired Varistor-NiZn Ferrite Multilayers," *Materials Research Bulletin*, Vol. 44, 2009, pp. 747-752.

[13] W. Yan, Q. Li, H. Zhong and Z. Zhong, "Characterization and Low-Temperature Sintering of $Ni_{0.5}Zn_{0.5}Fe_2O_4$ Nano-Powders Prepared by Rrefluxing Method," *Powder Technology*, Vol. 192, 2009, pp. 23-26.

[14] R. Jenkins and R. L. Snyder, "Introduction to X-ray Powder Diffractometry," John Wiley and Sons Inc., New York, 1996.

[15] I. Mihalca, A. Ercuta and C. Ionascu, "The Villari Effect in Fe–Cr–B Amorphous Ribbons," *Sensors and Actuators A*, Vol. 106, 2003, pp. 61-64.

[16] N. Spaldin, "Magnetic Materials: Fundamentals and Device Applications," Cambridge University Press, United Kingdom, 2003.

J. Electromagnetic Analysis & Applications, 2010, 2, 601-606
doi:10.4236/jemaa.2010.210079 Published Online October 2010 (http://www.SciRP.org/journal/jemaa)

An Analysis of Interference as a Source for Diffraction

Armand Waksberg

Consultant, Lasers and Electrooptics Montreal, Canada.
Email: chamonix@total.net

Received September 1st, 2010; revised September 29th, 2010; accepted October 6th, 2010.

ABSTRACT

An analysis is made of interference of two plane waves which in turn give rise to subsequent diffraction phenomena. This is done using two different approaches. One of them is straight forward but is difficult to interpret. The second is less conventional but more intuitive thus giving more insight into the process. The geometry is kept very simple to focus on the process itself. Both approaches give rise to the same results thus offering a choice in tackling such problems.

***Keywords*:** *Electromagnetic Wave Analysis, Diffraction Phenomena, Interference*

1. Introduction

Interference and diffraction theory have been developed as a result of the realization of the wavelike nature of light. This has led to the thousands of successful applications, ranging from the many forms of interferometers to the development of optical components such as Fresnel lenses and other Fourier transform components, making possible the wide field of present day Photonics.

The basics of interference and diffraction theory can easily be obtained from textbooks [1,2]. To get a better insight into these phenomena, however, would require a closer examination, such as, by looking at them from different perspectives.

The purpose of this paper is to provide such an insight by looking at a simple situation comprising an interference situation, which in turns gives rise to a diffraction phenomenon. The problem is then solved using two different approaches. Although the first is more straightforward, the results are difficult to interpret. The second, is less conventional but more intuitive. The geometry is kept very simple to focus on the process itself. It consists of a wall on which two plane waves intersect to form interference fringes, a slit in the wall through which the interference wave passes and a screen at a distance behind the wall which exhibits the resulting diffracted wave that was produced by the slit. Waveforms are calculated at the wall and at the screen for each of the two approaches and compared. The second approach is then used to offer an insight for the solution obtained by the first approach. The power transfer is calculated for each approach to ascertain that the process obeys conservation of energy.

As an example, we shall discuss how two beams intersecting and thus interfering at a point behave as they move away from it.

As both approaches give rise to the same results, a side benefit of this analysis is that it provides a choice in tackling such problems depending on the type of initial information that is supplied.

2. Configuration Selection

Referring to **Figure 1**, we assume two infinite plane waves with amplitude E_1 and E_2, polarized in the Y direction (which is perpendicular to the paper), with their normals in the XZ plane approaching an infinitely large wall in the XY plane at Z = 0. Their normals make an angle i and –i with the Z-axis respectively. It is further assumed that the wall has an infinitely long slit in the Y direction of width "a" along the X-axis centered at $X_w = 0$. On the right of the slit, a large screen, parallel to the wall, is placed at a distance "d" from it.

For discussion purpose, we have chosen the distance d so that the geometrical overlap of the two beans entering the slit and reaching the screen has a width a/2 along the X_s ordinate.

It is to be expected that there will be an interference effect at the wall due to the superposition of the two waves which will result in fringes on the wall. In particular, this interference field will penetrate the slit and end up on the

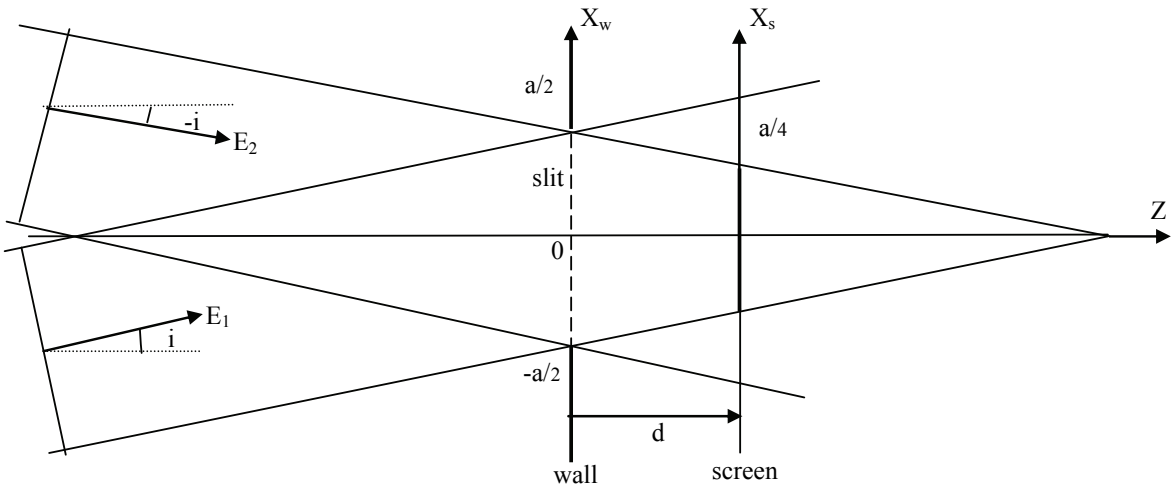

Figure 1. Two plane waves E_1 and E_2 intersect on a wall at Z = 0, enter through a slit of width and are projected on a screen at Z = d.

screen. We shall calculate, using two different approaches, the resulting field at the screen and compare the results.

2.1. Approach 1

Starting with what we consider the most straightforward approach, we shall calculate first the interference field at the slit. Since, on entering the slit, it is being sliced by its edges, which we assume to be very thin, we expect diffraction to take place. We shall then use diffraction theory to calculate the resulting field at the screen originating from this interference field.

2.2. Approach 2

We follow each plane wave separately, obtain their field strength at the slit, noting that each wave has been sliced by the slit, and calculate the resulting field at the screen as caused by diffraction. We end up with two separate diffracted fields at the screen originating from the two original plane waves. We then calculate the interference field resulting from their superposition. We compare the results with those of Approach 1 to ensure that they are the same.

3. Relevant Theory

Following Approach 1, let the two plane waves approaching the wall have a functional representation given by [3],

$$A(x,y,z,t) = Ae^{j(\omega t - kz)}e^{-j(kx\sin i + ky\cos i)} \quad (1)$$

$$B(x,y,z,t) = Be^{j(\omega t - kz)}e^{j(kx\sin i - ky\cos i)} \quad (2)$$

where A and B are amplitude constants proportional to the fields E_1 and E_2 respectively. They will be evaluated later. Since we want to calculate the interference field at the wall (including the slit), we know that $z_w = 0$. Also, since the field amplitude is invariable along the Y direction, we let y = 0. Adding Equations (1) and (2) we get the amplitude of the interference field at the wall to be,

$$C_w(x,t) = A_w e^{j(\omega t - kx\sin i)}(1 + \mathrm{Re}^{2jkx\sin i}) \quad (3)$$

where $R = B_w/A_w$.

To relate A_w and B_w to the actual field, we shall resort to the conservation of energy principle. To do this we note that the intensity at the wall of this interference field is given by the time average of the square of Equation (3) which is well known to require a factor of ½ to the result. The intensity is therefore given by,

$$I_w = \frac{|C_w(x)|^2}{2} = \frac{A_w^2}{2}\left[1 + R^2 + 2R\cos\gamma\right] \quad (4)$$

where $\gamma = 2kx\sin i$. The total power entering the slit per unit length in the Y direction is therefore,

$$P_w = \int_{-a/2}^{a/2} I_w dx = \frac{A_w^2 a}{2}\left[1 + R^2\right] + \sin(ka\sin i)/k\sin i \quad (5)$$

To simplify our interpretation, we want to examine only whole fringes. This will occur when the last term, which is associated with partial fringes, is made equal to zero. This occurs when $ka\sin i = n\pi$ where $n = 0,1,2,3...$ or

$$a_n = n\lambda/(2\sin i) \quad (6)$$

With n representing the number of whole fringes. The total power per unit length at the slit is,

$$P_w(n) = \frac{A_w^2 a_n}{2}\left[1 + R^2\right] \quad (7)$$

We are now prepared to relate A_w and B_w to the fields. Looking back at field E_1 in **Figure 1**, its related intensity is defined as the energy transmitted per sec per unit area normal to the direction of propagation. It is proportional to $E_1^2/2$. But the wall is not normal to the direction of the

plane wave. The intensity along the wall is spread out over a larger area by a factor of 1/cos i. The power associated with plane wave E_1 per unit of Y is therefore proportional to $E_1^2 \cos i/2$. Similarly, the power associated with E_2 is $\frac{E_2^2}{2}\cos i$. The total power entering the slit from both waves per units of Y is thus

$$\frac{E_1^2 a_n}{2}(1+R^2)\cos i \tag{8}$$

Comparing Equations (7) and (8) which should be equal for conservation of energy, we must have,

$$A_w^2 = E_1^2 \cos i \quad \text{and} \quad B_w^2 = E_2^2 \cos i \tag{9}$$

Before we can calculate the field at the screen using diffraction theory, we need the amplitude and phase of the field at the slit. We obtain it from Equation (3) by rewriting it as,

$$C_w(x) = A_w \left|D(x)\right| e^{j\Omega} \tag{10}$$

where $\left|D(x)\right| = \left|1+\mathrm{Re}^{j\gamma}\right|$ and $\Omega(x) = \beta(x) - kx\sin i$, and $\beta(x)$ is the argument of D(x), or the angle the phasor D(x) makes with the X-axis. The term $e^{i\omega t}$ has been omitted since it is common to all the expressions and is of no importance to calculate the amplitude at the screen. Since the field at the slit is being clipped by the edge of the slit, we shall use the Fresnel-Kirckhoff formulation of diffraction theory [1]. We assume that the two plane waves have their field polarized in the Y direction so that $E_x = E_z = 0$. Further, the slit at the wall is assumed to be infinite in length in the Y direction. This simplifies somewhat the mathematics since the field should be invariable in that direction. Consequently, we shall use the simplified one-dimensional expression [4],

$$C_s(x_s) = \frac{j}{2}\int_{-a_n/2}^{a_n/2} C_w(x_w)\{e^{-jk\rho_{sw}}/\sqrt{\rho_{sw}}\}\left[\cos\varphi_w + d/\rho_{sw}\right]dx_w \tag{11}$$

where C_s is the field disturbance resulting from that at the slit, d is the distance between the wall and the screen, $\rho_{sw} = [d^2 + (x_w - x_s)^2]^{1/2}$, φ_w is the angle between the wavefront at x_w and the wall normal. It can be obtained from the relation

$$\sin\varphi = \frac{1}{k}\partial\Omega(x)/\partial(x).$$

Equation (11) is a good approximation provided that $d > a$, $a > \lambda$, and the angle i is small.

Other approximations would provide similar results [5-7].

4. Numerical Calculations

For definiteness we let i = 10°, E_1 =1, a = 72 and d = 102 both in wavelength units. This will ensure the geometry given in **Figure 1**.

4.1. Approach 1

In this approach, we calculate first the amplitude of the interference field present at the slit. It is the resultant of the superposition of the two plane waves. It can be obtained from Equation (3) by taking its absolute value,

$$\left|C_w(x)\right| = A_w\left[1 + R^2 + 2R\cos\gamma\right]^{1/2} \tag{12}$$

This is the interference field, which is responsible for the visible fringes, given by Equation (4).

Plotting the interference field at the slit as a function of x_w, which is the normalized distance along the slit, we obtain waveform shown as curve (a) in **Figure 2**. we note first that there are 25 peaks present at the slit as should be expected, the slit extends in the range $-36 < x_w < 36$. for a total width of 72 wavelengths. The amplitude varies from 0 to 2 A_w.

We can now use the interference field Equation (3) at the slit to calculate how it is transformed when it reaches the screen. For this we use the appropriate diffraction expression Equation (11) since the field is sliced by the edges of the slit. It turns out that for R = 1, $\varphi_w = 0$ for all values of x_w. Using computer numerical calculations, we obtain the field at the screen which is plotted on the same graph in **Figure 2** as curve (b) for comparison purpose.

We observe that around the central portion of the screen, the waveform pattern is very similar in shape and amplitude to that at the slit. As we move away from this region, the field amplitude falls down to a level somewhat half-way down until around X_s = 50 when it decreases very quickly in amplitude towards zero. Also, the distance between peaks increased compared to that at the slit. To explain quantitatively the behaviour of the waveform from this approach is not simple. On the other hand, when Approach 2 is used, a much more intuitive derivation will permit a better understanding of the process.

4.2. Approach 2

In this approach, we follow each plane wave separately as they reach the slit. Since they are sliced by the slit, we can use diffraction theory to calculate their resulting fields at the screen. We then add these fields (which are phasors) to obtain the combined field. The results are then compared with that of Approach 1.

Starting with plane wave E_1, we notice that when it reaches the wall, its amplitude is obviously a constant, although its phase varies with X_w. C_w simplifies now to,

$$C_w(x) = A_w e^{-j2\pi x_w \sin i}. \tag{13}$$

This is shown in **Figure 3**-curve (a).

Since in this case φ = i = 10°, using Equation (11) we obtain the diffracted field amplitude at the screen shown as curve (b). As should be expected, this is a typical wave-

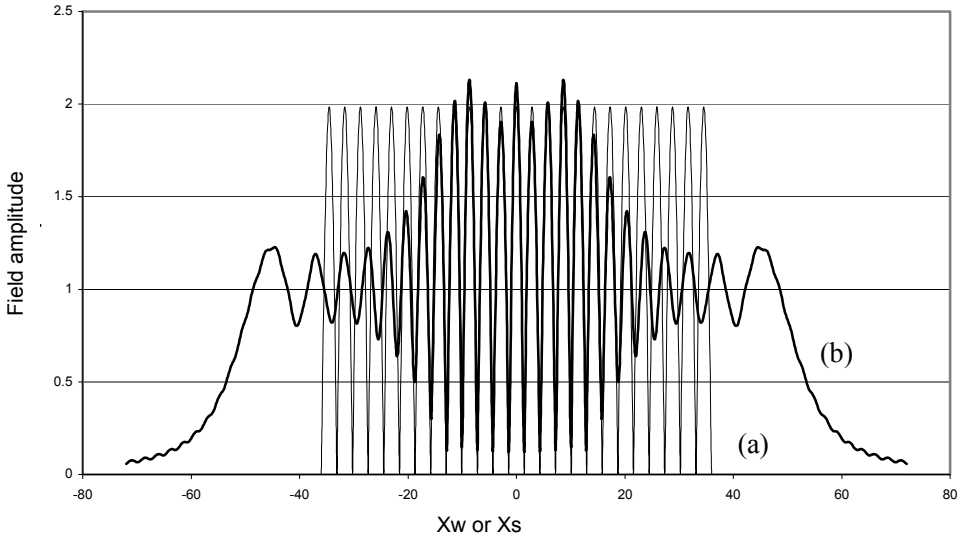

Figure 2. Field amplitude in arbitrary units of two plane waves E_1 and E_2 meeting at a slit as a function of position in wavelength units. (a) interference field at wall slit along Xw; (b) diffration field at screen along Xs.

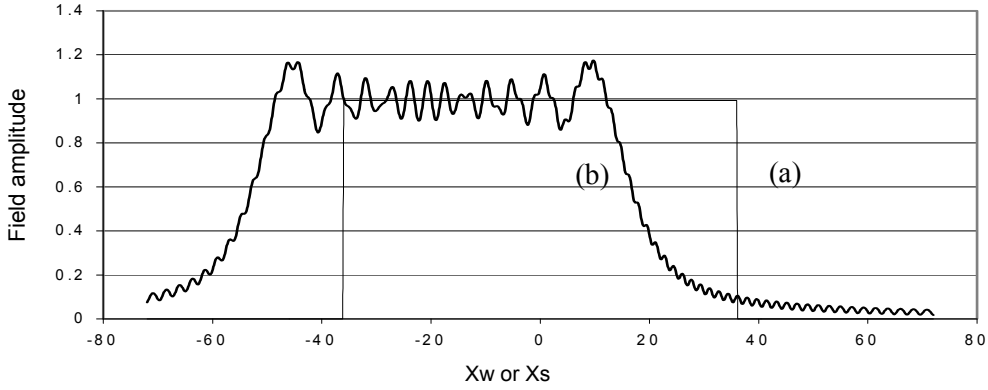

Figure 3. Field amplitude in arbitrary units of plane wave E_1 meeting at a slit as a function of position in wavelength units. (a) field at wall slit along Xw from plane wave E_1; (b) resulting diffration field at screen along Xs.

form of Fresnel diffraction by a slit. It is, however, displaced by 10^o to the left of center. Obviously, a similar waveform is produced by plane wave 2, except that it is displaced by the same amount to the right. Its function at the wall is,

$$C_w(x) = A_w e^{j2\pi x_w \sin i}. \quad (14)$$

If the two diffracted fields are added, the end result is shown in **Figure (4)** as curve (d). A comparison with **Figure 2** curve (b) shows that they are identical.

To get an intuitive understanding of that curve, we now plot on the same graph the waveforms of plane wave E_1 shown in **Figure 3** as curves (a) and (b). For reference purpose, curve (c) is added and is the interference field the two plane waves shown in **Figure 2** curve (a). Finally, we recall that in Section II we have selected the distance d so that the geometric overlap of the two waves at the screen covers only half the width of the slit. This is shown as region (e). We thus observe that, for the main diffraction curve (d):

1) At the edge of the waveform, on the left of the **Figure**, away from region (e), where there is no overlap, the shape follows almost exactly the waveform of a single plane wave - curve (b).

2) In region (e), the center portion where there is overlap, the shape is essentially that due to the sum of the two incoming waves.

3) In between those two regions, the wave progressively changes in shape and amplitude to blend from the overlap to the single wave region.

4) We should be gratified that our results show that in the region, away from (e), where there is no overlap, the waveform reverts to that of single plane waves. This is because we know from intuition, that if two beams cross

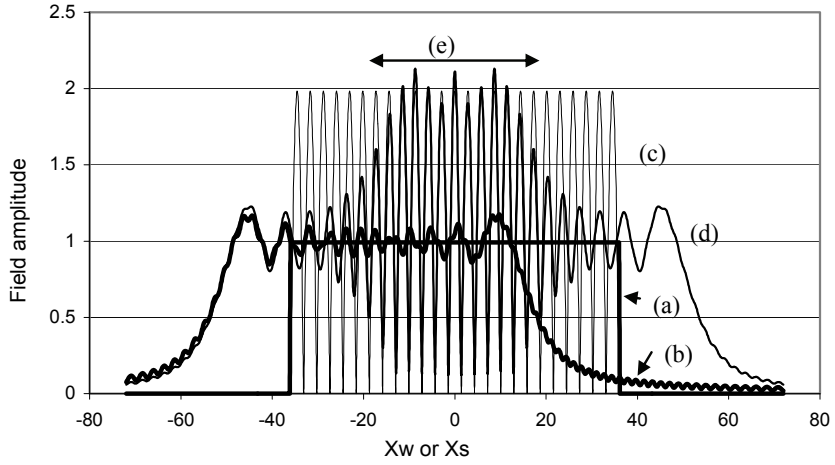

Figure 4. Field amplitude of plane wave(s) as a function of position for situations: (a) field at wall slit from plane wave E_1 along Xw; (b) diffraction field as a result of (a) at sceen along Xs; (c) interference field at wall slit along Xw resulting from both E_1 and E_2; (d) diffraction field at screen along Xs resulting from adding curve (b) from E_1 and its counter part from E_2; (e) geometric overlap of E_1 and E_2 at the screen.

one another, they will eventually carry on as if the interference region was not there. It should be emphasized, of course, that this is only true if the interference takes place in a vacuum where no other interaction takes place.

Approach II thus allows us to see why the shape of the diffracted wave derived in Approach I can be evolved from the diffracted waves produced by the two individual plane waves.

5) Power Transfer Considerations

We have shown, so far, that Approaches 1 and 2, although quite different, give out the same results as far as final waveforms at the screen are concerned. As a final check, we would like to ascertain that the power entering the slit is equal to the power reaching the screen for both Approaches for conservation of energy.

The initial power from the two incoming waves entering the slit per unit length in the Y direction is given by Equation (7). The intensity at the screen is given by

$$I_s = \frac{|C_s(x_s)|^2}{2}\cos\varphi_s(x_s) \tag{15}$$

where C_s is the total field obtained from Equation (11) for each of the approaches, while φ_s is the angle between the resulting field at x_s and the Z-direction. The total power per unit length in the Y direction in each case is then obtained by integrating,

$$P_s = \int_{-x_{s1}}^{x_{s1}} I_s(x_s)dx_s \tag{16}$$

Where x_{s1} is taken far enough from $x_s = 0$ that the field is negligible.

When the calculations are performed, it is found that the difference in power between the incoming power at the slit and that at the screen for both Approaches is of the order of 1%. This is well within the approximations expected from Equation (11).

6. Conclusion

We have considered interference theory resulting from two plane waves meeting at a slit, and on entering it, being subjected to the diffraction phenomenon. This was done using a simple geometry to focus on the process itself. Two approaches were selected, one more intuitive than the other. We have seen that they provide essentially the same results. Approach 2 which is more intuitive helps to understand the former which is more conventional but more difficult to visualize. It also demonstrate that interference effect in a vacuum, although manifesting itself mainly in a region of beam overlap, does not carry a permanent effect on the beams which revert back to their original behavior once they move far enough away from the overlapped region.

As a corollary to the calculations for both approaches, we have demonstrated, by an example, that the interference field which is made up of the superposition of two or more fields can be used as the starting source to calculate further diffraction effects caused by obstacles. On the other hand, if the components of the interference field reaching the obstacle are known, each of the components can be used to calculate its diffraction effect. The sum of the diffracted fields will then give rise to the same results as in the first case. Consequently, this suggests that a choice can be made in solving such problems based on the type of initial information that is supplied.

As a final remark, although we have considered in this paper only cases where R = 1 and 0, it can be shown that similar conclusions can be obtained for other values of R.

REFERENCES

[1] M. Born and E. Wolf, "Principle of Optics," Pergamon Press, New York, 1970.

[2] S. Silver, "Microwave Antenna Theory and Design," Dover, New York, 1965.

[3] C. Slater and N. Frank, "Electromagnetism," McGraw Hill, New York, 1947.

[4] A. Fox and T. Li, "Resonant Modes in a Maser Interferometer," *Bell System Technical Journal*, Vol. 40, 1961, pp. 453-488.

[5] K. Mielenz, "Algorithms for Fresnel Diffraction at Rectangular and Circular Apertures," *Journal of Research of the National Institute Standards and Technology*, Vol. 103, No. 5, 1998, pp. 497-509.

[6] K. Abedin, "Computer Simulation of Fresnel Diffraction from Rectangular Apertures and Obstacles Using the Fresnel Integrals Approach," *Optics and Laser Technology*, Vol. 39, No. 2, 2007, pp. 237-246.

[7] A. Waksberg, "FIR Laser Efficiency Enhancement by Double Resonance Tuning," *International Journal of Infrared and Millimetre Waves*, Vol. 26, No. 3, 2003, pp. 363-373.

Call for Papers

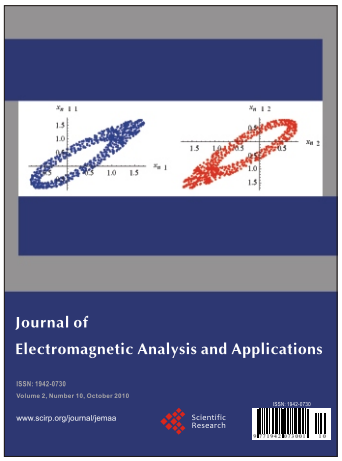

Journal of Electromagnetic Analysis and Applications

ISSN: 1942-0730 (Print), 1942-0749 (Online)
www.scirp.org/journal/jemaa

Journal of Electromagnetic Analysis and Applications(JEMAA) is a professional journal in the field of electromagnetic analysis, testing and application. The goal of this journal is to provide an international platform for engineers and academicians all over the world to promote, share, and discuss various new issues and developments in the field of electromagnetic. This journal is edited to encourage deeper understanding and greater effectiveness in theory analysis, testing, numerical calculation and engineering application that relevant electromagnetic fields.

Editors-in-Chief

Subject Coverage

JEMAA publishes four categories of original technical reports: papers, communications, reviews, and discussions. Papers are well-documented final reports of research projects. Communications are shorter and contain noteworthy items of technical interest or ideas required rapid publication. Reviews are synoptic papers on a subject of general interest, with ample literature references, and written for readers with widely varying background. Discussions on published reports, with author rebuttals, form the fourth category of JEMAA publications. Topics of interest include, but are not limited to:

- Electromagnetic Numerical Analysis
- Multiphysics Coupled Problems
- Electromagnetic Inverse Problems
- Electromagnetic Structure Optimization
- Test Electromagnetic Analysis Method
- Workshop Benchmark Problems
- Electromagnetic Devices
- Electromagnetic Compatibility
- Electromagnetic Nondestructive Testing
- Electromagnetic Material Modelling

Notes for Intending Authors

Submitted papers should not be previously published nor be currently under consideration for publication elsewhere. Paper submission will be handled electronically through the website. All papers will be peer reviewed. For more derails about the submissions, please access the website.

Website and E-Mail

http://www.scirp.org/journal/jemaa jemaa@scirp.org

J. Electromagnetic Analysis & Applications, **2010, 2, 581-606**
Published Online October 2010 in SciRes (http://www.SciRP.org/journal/jemaa)

TABLE OF CONTENTS

Volume 2 Number 10 **October 2010**

